A&A 490, 905–922 (2008)
DOI: 10.1051/0004-6361:200809839

Astronomy & Astrophysics

Absorption properties and evolution of active galactic nuclei

G. Hasinger[1,2]

[1] Max-Planck-Institut für extraterrestrische Physik, Gießenbachstr. 1, 85741 Garching, Germany
e-mail: ghasinger@mpe.mpg.de
[2] Institute for Astronomy, 2680 Woodlawn Drive, Honolulu, Hawaii 96822, USA

Received 24 March 2008 / Accepted 2 August 2008

ABSTRACT

Aims. Intrinsic absorption is a fundamental physical property for understanding the evolution of active galactic nuclei (AGN). Here we study a sample of 1290 AGN, selected in the 2–10 keV band from different flux-limited surveys with very high optical identification completeness.
Methods. The AGN were grouped into two classes, unabsorbed (type-1) and absorbed (type-2), depending on their optical spectroscopic classification and X-ray absorption properties, using hardness ratios. Utilising the optical to X-ray flux ratios, a rough correction was applied for the ∼8% redshift incompleteness still present in the sample. Then the fraction of absorbed sources was determined as a function of X-ray luminosity and redshift.
Results. The absorbed fraction decreases strongly with X-ray luminosity. This can be represented by an almost linear decrease from ∼80% to ∼20% in the luminosity range log L_X = 42–46 and is consistent with similar derivations in the optical and MIR bands. Several methods are used to study a possible evolution of the absorption fraction. The absorbed fraction increases significantly with redshift, which can be described by a power-law with a slope $\sim(1+z)^{0.62\pm0.11}$, saturating at a redshift of $z \sim 2$. A simple power-law fit $\sim (1+z)^{0.48\pm0.08}$ over the whole redshift is also marginally consistent with the data.
Conclusions. The variation in the AGN absorption with luminosity and redshift is described with higher statistical accuracy and smaller systematic errors than previous results. The findings have important consequences for the broader context of AGN and galaxy co-evolution. Here it is proposed that the cosmic downsizing in the AGN population is due to two different feeding mechanisms: a fast process of merger–driven accretion at high luminosities and high redshifts versus a slow process of gas accretion from gravitational instabilities in galactic discs rebuilding around pre-formed bulges and black holes.

Key words. galaxies: quasars: general – galaxies: Seyfert – X-rays: galaxies - X-rays: diffuse background

1. Introduction

In recent years it has become obvious that supermassive black holes at the centres of galaxies must play an important role in the evolution of galaxies. There is a strong correlation between the black hole mass and global properties of its host galaxy spheroid, like the bulge luminosity (Kormendy & Richstone 1995; Magorrian et al. 1998) and the stellar velocity dispersion, i.e. the M_{BH}-σ relation (Ferrarese & Merritt 2000; Gebhardt et al. 2000). At the same time, evidence is mounting that AGN and galaxies in general undergo very similar evolution patterns. The peaks of AGN activity and star formation occur in the same redshift range (z = 1.5–2), and there is a similar dramatic decline towards low redshift. Moreover, the mass density of local dormant supermassive black holes in galaxy centres is consistent with the mass density accreted by AGN throughout the history of the Universe (Marconi et al. 2004; Merloni 2004), yielding further evidence of a tight link between nuclear black hole activity and the growth of galaxy bulges. Many recent theoretical models propose that feedback from the growing supermassive black holes plays an important role in linking the properties and evolution of central black holes and their host galaxy (Silk & Rees, 1998; Di Matteo et al. 2005). The feedback from powerful AGN can quench star formation and inhibit the growth of the most massive galaxies (Scannapieco & Oh 2004), and this effect is indeed required to match the results of hydrodynamical simulations to the observed bright end of the galaxy luminosity functions (Springel et al. 2006; Hopkins et al. 2006).

A strong dependence of the AGN space density evolution on X-ray luminosity has been found, the so-called luminosity-dependent density evolution (LDDE) with a clear increase in the peak space density redshift with increasing X-ray luminosity, both in the soft X-ray (0.5–2 keV) and the hard X-ray (2–10 keV) bands (Miyaji et al. 2000; La Franca et al. 2002; Cowie et al. 2003; Ueda et al. 2003; Fiore et al. 2003; Hasinger et al. 2005). This AGN cosmic downsizing evolution, which recently has also been confirmed in the radio and optical bands (Cirasuolo et al. 2002; Bongiorno et al. 2007) is very similar to the downsizing of the faint galaxy population that shows a smooth decline in their maximum luminosity with decreasing redshift for $z < 1$ (Cowie et al. 1996). The observed cosmic downsizing indicates that active star formation and black hole growth shift to lower mass galaxies throughout the evolution of the Universe, which is somewhat counter-intuitive to the standard cold dark matter scenario, where large-scale structure evolves hierarchically from small to larger entities. The AGN results indicate a dramatically different evolutionary picture for low-luminosity AGN compared to the high-luminosity QSOs. While the rare, high-luminosity objects can form and feed very efficiently, possibly by multiple mergers rather early in the universe (see e.g. Li et al. 2006), with their space density declining more than two orders of magnitude at redshifts below z = 2, the bulk of the AGN has to wait much longer to grow or to be activated, with a decline in space density by less than a factor of 10 below a redshift of one. The late evolution

of the low-luminosity Seyfert population is very similar to what is required to fit the mid-infrared source counts and background (Franceschini et al. 2002) and also the bulk of the star formation in the Universe (Madau 1996), while the rapid evolution of powerful QSOs traces the history of formation of massive spheroids more closely (Franceschini et al. 1999). This could indicate two different modes of accretion and gas supply for the black hole growth with substantially different accretion efficiency (see e.g. the models of Cavaliere & Vittorini 2000; Di Matteo et al. 2003; Merloni 2004; Menci et al. 2004).

A large fraction of the accretion in the Universe is obscured by intervening gas and dust clouds. Indeed, the spectrum of the X-ray background can very well be described by a combination of absorbed and unabsorbed AGN evolving through cosmic time (e.g. Comastri et al. 1995; Gilli et al. 2007, hereafter GCH07). However, one of the major uncertainties in the study of AGN evolution and black hole growth is the unknown distribution of absorbing column densities and its dependence on AGN luminosity and on cosmic time. Indeed, studies of local Seyfert 2 galaxies have shown that a large fraction of these (~40%) are Compton-thick (Risaliti et al. 1999) and thus practically absent in X-ray surveys. Therefore, the luminosity-dependent AGN evolution picture could be significantly biased by systematic selection effects (see e.g. Treister et al. 2004). Ueda et al. (2003) have for the first time found a significant decrease in the fraction of obscured AGN with increasing X-ray luminosity, and similar results have been obtained almost simultaneously from independent X-ray selected AGN samples by Steffen et al. (2003) and Hasinger (2004). Recently, these trends have been confirmed in optically selected AGN observed in the SDSS (Simpson 2005) and with *Spitzer* in the MIR (Maiolino et al. 2007; Treister et al. 2008), indicating a breakdown of the standard AGN unification model (Antonucci 1993; see also Ballantyne et al. 2006). The possible evolution of the fraction of obscured sources with redshift is still a matter of debate in the literature. A tentative redshift dependence of the obscured fraction was reported by La Franca et al. (2005). Other authors (e.g. Ueda et al. 2003, GCH07) did not find a significant redshift dependence. Recently, Ballantyne et al. (2006) and Treister & Urry (2006) have presented evidence for a shallow increase in the absorbed fraction with redshift. The different results could indicate both systematic and statistical effects in the analysis.

In this paper the best available AGN samples selected in the 2–10 keV X-ray band with the highest redshift completeness possible have been compiled, resulting in 1406 objects, of which more than 92% have redshift information, mainly from optical spectroscopy. This allows for the best combination so far of object statistics and completeness in any hard X-ray selected AGN sample. In Sect. 2 the hard X-ray selected AGN sample is described in detail. Section 3 discusses the classification criteria used to distinguish between type-1 (unabsorbed) and type-2 (absorbed) AGN. Section 4 presents the number counts of the different source populations and Sect. 5 elaborates on a method of correcting for the small, but significant redshift incompleteness in the sample. Section 6 is the main body of the paper that discusses the luminosity- and redshift dependence of the absorbed AGN fraction. Finally, the results are discussed in Sect. 7 and summarised in Sect. 8. Throughout this work, a cosmology with $\Omega_m = 0.3$, $\Omega_\Lambda = 0.7$, and $H_0 = 70$ km s^{-1} Mpc^{-1} is used.

2. The hard X-ray selected AGN sample

For studying the AGN X-ray absorption and its cosmological evolution, well-defined flux-limited samples of AGN with a high redshift completeness have been selected in the 2–10 keV band, with flux limits and survey solid angles ranging over five and six orders of magnitude, respectively.

A total of 1290 X-ray selected AGN were compiled from ten independent samples containing a total of 1406 X-ray sources selected in the 2–10 keV band. Of these, 1106 have reliable optical spectroscopic redshift identifications. For the optically fainter sources, in particular in those samples with fainter X-ray flux limits, it becomes increasingly difficult to obtain reliable spectroscopic redshifts and classifications. However, for survey fields with substantial multi-band photometric coverage, e.g. the GOODS North and South areas in the CDF-N and CDF-S, respectively, it has been shown that photometric redshifts can be used reliably (Zheng et al. 2004; Mainieri et al. 2005; Grazian et al. 2006). A total of 188 photometric redshifts are used in the samples in Table 1. The number of unidentified sources that do not have a reliable redshift determination, either through spectroscopy or through photometry, but nevertheless have optical or NIR counterparts, is only 112, yielding an identification fraction of 92%. To control systematic redshift incompleteness effects, crude redshifts have been estimated for the unidentified sources, using the X-ray to optical flux ratio, following Fiore et al. (2003). The surveys utilised in this work are summarised in Table 1. Please note that the number of type-1 and type-2 AGN in Table 1 includes the photometric and crude redshifts and that other source classes like galaxies, stars, clusters, etc. are omitted here.

For several surveys a limit in X-ray flux or off-axis angle had to be chosen a posteriori, based on optical completeness criteria, thus maximising the number of sources with redshifts, while simultaneously minimising the number of unidentified objects. For the purpose of this paper, all X-ray fluxes in the different samples have been converted to observed 2–10 keV fluxes assuming the same spectral index for all sources within each sample (see below). While it is in principle possible to attempt a correction to *intrinsic*, *restframe* 2–10 keV fluxes for each source individually, using spectral indices and hydrogen column densities determined from direct spectral fits or hardness ratios, this has not been done here for several reasons. This procedure introduces additional statistical errors into the flux determination due to the uncertainty in the spectral parameters. Most of the sources in the flux-limited samples used here contain very few X-ray photons so that only a crude hardness ratio is available that does not allow absorption and spectral slope to be determined independently, let alone more complicated spectral models. While these uncertainties have a relatively weak effect on the flux observed in the source detection band, extrapolations to the source restframe would amplify these errors. For the comparison with theoretical models, it is easier to fold these observational effects into the predictions instead of trying to correct the observations. Therefore all fluxes and luminosities refer throughout this paper to observed quantities in the observed 2–10 keV band. Below we summarise our sample selection and completeness for each survey. Figure 1 gives the solid angle versus flux curve for the individual surveys and the total sample used.

2.1. The HEAO-1/Grossan sample

Shinozaki et al. (2006) have selected a flux-limited sample of 49 AGN from the *HEAO-1* all-sky-survey, which has also been used in the Ueda et al. (2003) analysis. For the brighter part of the sample (28 sources with 2–10 keV fluxes larger than 2.7×10^{-11} erg cm^{-2} s^{-1}), they used the classical Piccinotti et al. (1982) catalogue based on the *HEAO-1* A2 instrument

Table 1. The hard X-ray sample.

Survey	Solid angle [deg^2]	$S_{\rm lim}$ [erg cm^{-2} s^{-1}]	$N_{\rm tot}$	$N_{\rm unid}$	$N_{\rm zph}$	$N_{\rm AGN1}$	$N_{\rm AGN2}$
HEAO1/Grossan	2658–22 000	$(1.0–2.7) \times 10^{-11}$	50	0	0	41	9
AMSS/ALSS	~4.8–90.8	$(0.11–2.1) \times 10^{-12}$	139	1	0	88	37
HBSS	25.17	2.15×10^{-13}	67	2	0	42	20
XMS	2.46–3.80	$(3.30–9.36) \times 10^{-14}$	144	13	0	111	25
CLASXS	0.4	1.3×10^{-14}	112	19	0	67	41
HELLAS2XMM	0.21–0.90	$(1.0–3.7) \times 10^{-14}$	171	27	0	115	51
SEXSI	0.046–0.979	$(0.51–5.72) \times 10^{-14}$	252	40	0	151	90
LH/XMM	0.1056	5.1×10^{-15}	64	4	11	40	20
CDF-S	0.012–0.0873	$(0.44–1.49) \times 10^{-15}$	239	4	66	80	131
CDF-N	0.0075–0.0873	$(0.18–1.49) \times 10^{-15}$	284	8	111	99	141
Total			1406	112	188	759	531

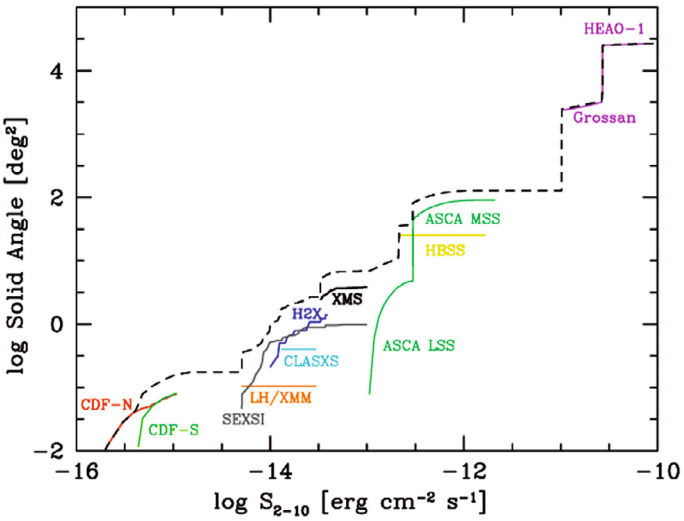

Fig. 1. The solid angle as a function of flux limit covered in the ten independent surveys utilised in this analysis.

on a solid angle of 2.7×10^4 deg^2. At fainter fluxes (above 10^{-11} erg cm^{-2} s^{-1}), they augmented this by sources from the catalogue derived by Grossan (1992) through a crosscorrelation of the *HEAO-1* A1 (Large-Area Counter) and A3 (Modulation Collimator) instruments (the *HEAO-1 A3 MC LASS* Catalog). 21 sources from the Grossan sample were selected in a sky area of 5105 deg^2 with particularly high identification completeness. Shinozaki et al. have originally excluded the source H1443+421 (1H1448+415) from their low-redshift sample. However, it turned out later that the most likely identification for this source is the ROSAT source 1RXS J144645.8+403510, listed as a QSO at $z = 0.267$ in the Simbad data base (Miyaji 2007, priv. comm.). Including this object, the total number of HEAO-1 AGN used in this analysis is 50. The fluxes of the Grossan objects have been corrected to first order for the bias related to confusion noise by Shinozaki et al.; while these authors give fluxes for their sample based on individual spectral slopes, for the analysis presented here, all fluxes have been converted assuming a power-law spectrum with a photon index of 1.65.

2.2. The ASCA Medium Sensitivity and Large Sky Surveys (AMSS/ALSS)

For the *ASCA* Large Sky Survey and Medium Sensitivity Survey, the same subsamples as defined by Ueda et al. (2003) have been used in this analysis. The *ASCA* Large Sky Survey (LSS) is a contiguous 7 deg^2 strip in the north Galactic pole region surveyed with the ASCA GIS and SIS instruments (Ueda et al. 1999). Optical identifications for 34 sources above a 2–10 keV flux limit of 1.2×10^{-13} erg cm^{-2} s^{-1} are given by Akiyama et al. (2000) and updates in Ueda et al. (2003). The *ASCA* Medium Sensitivity (GIS) survey is based on the two X-ray catalogues published by Ueda et al. (2001, 2005). Spectroscopic optical identifications are from Akiyama et al. (2003) for the northern subsample and from Ueda (2007, priv. comm.) for the southern subsample. In total the *ASCA* Large Sky and Medium Sensitivity Surveys contain 139 objects, of which 125 are AGN and only one source remains unidentified.

2.3. The XMM-Newton Hard Bright Serendipitous Sample (HBSS)

The HBSS is a subset of the larger *XMM-Newton* Bright Serendipitous Survey (Della Ceca et al. 2004) carried out by the *XMM-Newton* Survey Science Center (Watson et al. 2001) consortium. It is a complete flux-limited sample of bright X-ray sources ($F_x > 7 \times 10^{-14}$ erg cm^{-2} s^{-1}) at high galactic latitude ($|b| > 20$ deg), selected in the 4.5–7.5 keV energy band. The HBSS was designed to have a flat sky coverage of 25.17 deg^2 at a fixed MOS2 count rate limit of 2×10^{-3} cts s^{-1} in the 4.5–7.5 keV band. The MOS2 count rates in the HBSS were converted to observed fluxes in the 2–10 keV band, assuming a photon power-law index of 1.9 (using a count rate to flux conversion factor of 1.077×10^{-11} erg cm^{-2} cts^{-1}. The flux limit of the HBSS is therefore 2.15×10^{-13} erg cm^{-2} s^{-1}. The HBSS sample is now almost completely optically identified, leaving only 2 out of 67 objects unidentified and thus yielding a spectroscopic completeness of ~97% (Caccianiga et al. 2000; Della Ceca et al. 2008).

2.4. The XMM-Newton Medium-sensitivity Survey (XMS)

The *XMM-Newton* Medium-sensitivity Survey (XMS, Barcons et al. 2007) is a serendipitous X-ray survey and optical identification programme of sources with intermediate X-ray fluxes discovered in 25 *XMM-Newton* high Galactic latitude fields covering a sky area of ~3 deg^2. For this analysis the XMS-H sample was used, selected in the 2–10 keV band. The original Barcons et al. sample contains 159 sources with 2–10 keV fluxes

Table 2. Identification completeness in XMS fields used in this study.

Number of unidentified Sources	0	1	2	3
Number of Fields	16	6	2	1

$>3.3 \times 10^{-14}$ erg cm^{-2} s^{-1} with a spectroscopic identification fraction of 83% (27 unidentified sources). However, the actual spectroscopic completeness limit varies from field to field. In order to optimise the redshift completeness of the XMS, a strategy was chosen, which maximises the sample of identified sources, while minimising the number of unidentified sources. There are 15 fields that are either completely identified down to the survey flux limit or have a small number of unidentified sources significantly brighter than the flux limit. For those fields, the flux limit was maintained and the unidentified sources enter the sample for this analysis. For the remaining 10 fields, unidentified sources have the lowest flux in the particular subsample. In these cases the unidentified sources were excluded. The flux limit for this field was then raised to the geometric mean between the flux of the first unidentified and the last identified source in order to avoid the gerrymandering effect introduced by defining a post-facto flux limit (see also Hasinger et al. 2005). This effect can be explained in the following way: if one has a pre-defined flux limit for a (sub)survey, then the faintest source in the sample is expected to lie somewhat above this flux limit. If, on the other hand, the flux limit would be defined post facto exactly at the flux of the faintest identified source, a small bias is introduced. Defining the flux limit between two adjacent sources in the original sample minimises this bias. Table 2 summarises the unidentified source statistic for the XMS fields. This way a cleaner XMS sample could be defined, comprising 144 objects and almost half the number of unidentified sources, i.e. achieving an identification fraction of 91%. The survey solid angle has been corrected accordingly (see Fig. 1).

2.5. *The* Chandra *Large Synoptic X-ray Survey (CLASXS)*

CLASXS is a large contiguous survey consisting of nine intermediate-depth *Chandra* pointings in a 3×3 grid in the Lockman Hole (~2.5 deg northwest of the original LH deep survey, see below), in a region with the lowest Galactic neutral hydrogen column density (Lockman et al. 1986). A catalogue of 525 X-ray sources discovered in CLASXS is given in Yang et al. (2004). Steffen et al. (2004) present optical identifications and 271 spectroscopic redshifts for the CLASXS, yielding an overall spectroscopic completeness of 52%. For the work discussed here, the sample of 319 sources detected with a signal-to-noise ratio $SNR \geq 2.0$ in the hard band (2–8 keV) was utilised. Down to the original survey flux limit of 2.1×10^{-15} erg cm^{-2} s^{-1}, there are 138 objects without redshifts. To obtain an acceptable unidentified fraction, the original catalogue had to be cut at a substantially higher flux limit of 1.3×10^{-14} erg cm^{-2} s^{-1}, yielding a sample of 103 sources, of which 20 remain unidentified. The redshift completeness is thus 81%.

2.6. *HELLAS2XMM*

HELLAS2XMM (Baldi et al. 2002) is a serendipitous survey based on suitable *XMM-Newton* pointings (complementary to the XMS) and building on the experience of the original *BeppoSAX* High Energy Large Area Survey (HELLAS). Fiore et al. (2003) present optical identifications and spectroscopic redshifts for 122 sources selected in the 2–10 keV band in five *XMM-Newton* fields, covering a survey area of 0.9 deg^2. For the distinction between absorbed and unabsorbed sources (see below), hardness ratios from Perola et al. (2004) were used, kindly provided by M. Brusa (2007, priv. comm.). Originally Fiore et al. published optical spectroscopic redshift identifications for 97 of their objects, yielding a redshift completeness of ~80%. Later Maiolino et al. (2006) presented additional redshifts from VLT NIR spectroscopy of optically extremely faint objects for two additional sources. Both Fiore et al. and later Mignoli et al. (2004) tried to estimate redshifts for the remaining, optically faint, unidentified sources. Fiore et al. employed the optical to X-ray flux ratio to obtain crude redshift information. Mignoli et al. used further, deep NIR imaging with ISAAC at the VLT of optically very faint counterparts in HELLAS2XMM. Using both the $R - K$ colours and the morphological information, they estimated photometric lower limit redshifts for 9 of the originally unidentified sources in the Fiore et al. sample, also yielding consistent redshifts for the two objects later identified in the Maiolino et al. NIR spectroscopy. In Sect. 5 the X-ray/optical flux ratio will be used to estimate crude redshifts for all unidentified sources in this study, but for the moment the crude redshifts for HELLAS2XMM are not taken into account in the sample completeness. However, a 2–10 keV flux limit of 10^{-14} erg cm^{-2} s^{-1} was chosen, thus removing the faintest 4 sources, which are all unidentified.

Recently Cocchia et al. (2007) have published photometry and spectroscopic redshifts in five additional HELLAS2XMM fields providing 59 new redshift identifications for the sample of 110 new sources. To maximise the redshift completeness of this sample, a procedure similar to the one used for the XMS was applied (see above). However, because in this case some fields were observed or identified only outside the central image region, an inner and an outer off-axis cut had to be applied in addition to a flux cut. As in the case of the XMS, the flux and off-axis limits were chosen in the geometric mean between the last identified and the first unidentified object. This way flux limits between 1.18 and 2.56×10^{-14} erg cm^{-2} s^{-1} were chosen for the different fields, and the total additional solid angle collected this way was 0.48 deg^2. The sky coverage of the survey (see Cocchia et al. 2007) was corrected accordingly. In this way an additional 49 sources with only 4 unidentified objects could be added to the sample. This leaves in total 171 sources, of which 27 remain unidentified. The redshift completeness in this subsample of HELLAS2XMM is thus 84%.

2.7. *The Serendipitous Extragalactic Source Identification* SEXSI *Programme*

SEXSI is a serendipitous survey based on 27 *Chandra* archival, high Galactic latitude pointings followed up spectroscopically with the Keck telescopes. Eckart et al. (2006) presented spectroscopic redshift identifications for 438 objects out of a total sample of 1034 sources selected in the 2–10 keV band, yielding an original identification completeness of 42% over a survey area of ~2 deg^2. For their sample Eckart et al. have utilised the *Chandra* sources over the whole field-of-view (FOV) and to the full sensitivity limit of their observations. To optimise the completeness of the SEXSI sample to be utilised for this study, the original sample was cut both in off-axis angle and in flux limit, following a procedure similar to the one described above for the XMS. At the outset, the whole sample was reduced to off-axis angles below 8.31′, thus concentrating on the inner part of the *Chandra* FOV with higher angular resolution and sensitivity. Then, a limit was defined separately for each of the 27 SEXSI pointings both

Table 3. Identification completeness in SEXSI fields used in this study.

Unidentified Sources	0	1	2	3	4	5	not used
Number of Fields	1	8	5	3	2	1	7

in flux and in off-axis angle so as to limit the fraction of unidentified sources to <80% in each field. A total of 7 out of the original 27 fields had to be rejected, because this condition could not be fulfilled. The remaining fields had between 0 and 5 unidentified sources left (see Table 3). To avoid biases in the effective area versus solid angle curve introduced by this gerrymandering procedure, both the flux limit and the off-axis limit for each pointing was defined as the geometric mean between the corresponding values of the last identified and the first unidentified source in each field (sorted in flux or in off-axis angle, respectively). In this way, a total number of 252 objects were retained for the SEXSI subsample used in this study, of which 40 remain unidentified, yielding a spectroscopic completeness of ∼84% over a solid angle of ∼1 deg^2.

2.8. *Deep XMM-Newton survey of the Lockman Hole (LH/XMM)*

The Lockmam Hole (LH/XMM) has been observed by *XMM-Newton* 17 times during the PV, AO-1 and AO-2 phases of the mission, with total good exposure times in the range 680–880 ks in the PN and MOS instruments (see Hasinger et al. 2001, 2004; Worsley et al. 2004; Brunner et al. 2008 for details). Spectroscopic optical identifications of the *ROSAT* sources in the LH have been presented by Schmidt et al. (1998) and Lehmann et al. (2000). A catalogue from the *XMM-Newton* PV phase was published by Mainieri et al. (2002) and some photometric redshifts have been discussed in Fadda et al. (2002). Here objects were selected from 266 sources detected in the hard band of the 637 ks dataset (Brunner et al. 2008) with additional spectroscopic identifications obtained with the DEIMOS spectrograph on the Keck telescope in spring 2003 and 2004 by Schmidt and Henry (Szokoly et al. 2008) and also including a number of new photometric redshifts (Mainieri 2007, priv. comm.). To maximise the spectroscopic/photometric completeness of the sample, objects were selected in two off-axis intervals with different 2–10 keV flux limits: 2.5×10^{-14} erg cm^{-2} s^{-1} for off-axis angles in the range 11.0–14.3 arcmin and 5×10^{-15} erg cm^{-2} s^{-1} for off-axis angles smaller than 11 arcmin. The total number of sources in the LH/XMM survey is 64, with 4 objects still unidentified.

2.9. *The* Chandra *Deep Field South (CDF-S)*

For this study the catalogue of Giacconi et al. (2002), based on the 1 Ms observation of the CDF-S (Rosati et al. 2002), was used and expanded with two additional objects from the catalogue derived from the same data set by Alexander et al. (2003), which were confused in the original Giacconi et al. catalogue, but formally fulfill the same detection criteria. One source (XID 527) was removed, because it was identified with the jet of an extended radio source already matched with another X-ray source (Mainieri et al. 2008). The 239 sources detected significantly in the 2–10 keV band (signal to noise ratio >2.0) and within an off-axis angle of 10 arcmin were thus selected. The solid angle area curve given in Giacconi et al. (2002) was used, but truncated at an off-axis angle of 10 arcmin.

Spectroscopic identifications in the CDF-S have originally been obtained by Szokoly et al. (2004) with the FORS instruments at the ESO VLT, yielding a spectroscopic completeness of ∼48% in the hard band. Additional spectroscopic redshifts of CDF-S X-ray sources were obtained with the ESO VLT as part of the VVDS and GOODS surveys and have been collected in the catalogue of Grazian et al. (2006). In the meantime more spectroscopic redshifts have been obtained both with VIMOS and with FORS2 at the VLT through the GOODS programme (PI: Cesarsky) and the CDFS follow-up (PI: Bergeron). The spectroscopic follow-up observations of the Extended Chandra Deep Field South (ECDFS, see Lehmer et al. 2000) have also yielded additional identifications in the CDF-S proper, both from the VLT and from Keck (Szokoly & Silverman 2007, priv. comm.). For the 239 CDFS sources selected for this study, we therefore have the following breakdown of spectroscopic redshifts: 111 objects from Szokoly et al. (2004), 30 redshifts from the public GOODS data releases based on VLT FORS and VIMOS spectroscopy (Vanzella et al. 2008; Popesso et al. 2008), 13 and 4 objects from the ECDFS spectroscopic follow-up using VIMOS at the VLT and DEIMOS at the Keck telescopes, respectively (Silverman, Szokoly et al. 2007, priv. comm.), 7 objects from the K20 survey (Mignoli et al. 2005), and 3 redshifts from the VVDS (Le Fevre et al. 2004). This subsample of the CDF-S therefore has a spectroscopic completeness of 71%.

The field is also included in the COMBO-17 intermediate-band survey, which gives very reliable photometric redshifts for optically brighter sources (Wolf et al. 2004). A total of 9 COMBO-17 redshifts were used here. The CDF-S has also been surveyed by the HST ACS as part of the GOODS (Giavalisco et al. 2004) and GEMS (Rix et al. 2004) projects. Very deep NIR photometry has been obtained with the ISAAC camera at the VLT as part of the GOODS project (Mobasher et al. 2004). Finally, the GOODS area has been covered in the MIR spectral range by deep Spitzer observations. The CDF-S therefore offers the highest quality photometric redshifts of faint X-ray sources, which were originally derived by Zheng et al. (2004) and Mainieri et al. (2005). More recently, Grazian et al. (2006) have derived photometric redshifts in the GOODS CDF-S area including the Spitzer MIR photometry. Using the better infrared photometry, Brusa et al. (2008) have obtained new, unambiguous identifications for two objects, which originally had two plausible counterparts in Szokoly et al. (2008). For the X-ray source with XID 201 the spectroscopic redshift $z = 0.679$ in Szokoly et al. was given for the object (b) in the *Chandra* error circle, while the Spitzer data indicate that the object (a) with a photometric redshift $z_p = 2.88$ (Grazian et al.) is the correct counterpart. A similar situation exists for the X-ray source with XID 218, where the spectroscopic redshift $z = 0.479$ for object (a) has been replaced with a photometric redshift $z = 2.27$ for object (b) in the error circle. Several of the original Zheng et al. photometric redshifts have been superseded by the better Grazian et al. values; however, the overall redshift distribution for the CDF-S did not change significantly using the new data. For this analysis 27 photometric redshifts taken from Grazian et al. were used, and 33 redshifts with a photometric quality $Q \geq 0.2$ from Zheng et al. Four objects had too low a quality in their photometric redshift solution or no data at all and thus remain unidentified, yielding an excellent overall redshift completeness of 98%.

2.10. Chandra *Deep Field North (CDF-N)*

A sample of 284 X-ray sources significantly detected in the hard band and inside an off-axis angle of 10 arcmin were selected from the 2 Ms CDF-N source catalogue by Alexander et al. (2003). The solid angle area curve given by these authors

was truncated at 10 arcmin off-axis angle as well. For uniformity with the other samples used in this study, the CDF-N fluxes were recomputed from the count rates given in Alexander et al., assuming a photon spectral index of 1.4 for all sources. To convert the count rates, which are extracted in the 2–8 keV band, into 2–10 keV fluxes, a counts to flux conversion factor of 2.88×10^{-11} erg cm^{-2} was used.

Optical spectroscopic identifications in the CDF-N have been compiled from various catalogues in the literature. The largest number of spectroscopic redshifts (114) were taken from Barger et al. (2001, 2003), and 33 objects from Cohen et al. (2000). Another 12 objects were taken from various publications summarised in the NASA Extragalactic Database (Bauer et al. 2002; Chapman et al. 2003; Cowie et al. 2004; Cristiani et al. 2004; Smail et al. 2004; Swinbank et al. 2004; Wirth et al. 2004) and 6 objects were provided by Capak (2007, priv. comm.). The redshift of the object VLAJ123642+621331, originally placed at $z = 4.424$ by interpreting the single emission line in its spectrum as Lyα (Waddington et al. 1999), has been corrected to $z = 1.770$, because the photometric redshift of this source (Capak 2007, priv. comm.) fits much better, if the line is interpreted as [OII]3727. With the set of 165 spectroscopic redshifts available, this CDF-N subsample has a spectroscopic completeness of 58%. Photometric redshifts for the CDF-N have been kindly provided for this study by Capak (2007, priv. comm.). They are described to some degree in Barger et al. (2003) and allow this field to be exploited to its full depth. Here 111 objects with photometric redshift errors $\Delta z < 1.5$ have been used, leaving only 8 objects unidentified. The CDS-N sample utilised here therefore has a redshift completeness of 97%, very similar to the CDF-S discussed above.

3. AGN classification criteria

A crucial prerequisite for the analysis presented here is the distinction between absorbed and unabsorbed X-ray sources. This is, however, not a trivial task and a matter of some controversy in the literature. The classical distinction between optically unobscured (type-1) and obscured (type-2) AGN is made through optical spectroscopy. Optical type-1 AGN have broad permitted emission lines (>2000 km s^{-1}), while optical type-2 AGN do not show broad permitted lines, but still have high-excitation narrow emission lines. Therefore many works in the field mainly use the presence of broad lines as discriminator and classify objects as type-1 AGN only if they have broad lines (see e.g. Barger et al. 2005; Treister & Urry 2006). However, this AGN classification scheme breaks down, when the optical spectrum is insufficient to accurately determine the emission line widths. At high redshifts and low luminosities, there are several effects that compromise the optical classification. First, in general high-redshift objects are faint, so that they require very long observing times on large telescopes to obtain spectra of sufficient quality to unambiguously discern broad emission line components. Secondly, there are redshift ranges, where the strong classical broad lines shift out of the observed spectroscopic optical bands. Thirdly, and probably most importantly, at high redshifts the spectroscopic slit includes the light of the whole host galaxy, which dilutes the spectrum of the AGN nucleus. Depending on the ratio between nuclear and host luminosity, the host galaxy can easily outshine the AGN nucleus, rendering the AGN invisible in the optical light. This effect has been demonstrated for local bona fide bright Seyfert galaxies, where the emission lines are diluted in the host galaxy light when the integral light of the galaxy is sent through the spectrograph slit (see e.g. Moran et al. 2002) and is the main reason that X-ray samples are much more efficient in picking up low-luminosity AGN at high redshift.

The optical spectroscopic AGN classification is mainly based on broad permitted lines in the restframe blue and ultraviolet part of the spectrum. The amount of obscuration in the optical spectrum can be estimated using e.g. the Balmer decrement. At $N_{\rm H} > 3 \times 10^{21}$ cm^2 the broad UV lines are usually suppressed and only narrow lines remain.

In principle, a classification purely based on X-ray properties would be possible. High hydrogen column densities block soft X-rays; therefore, a suitable AGN classification scheme in X-rays could involve the column density $N_{\rm H}$ that can be determined from the X-ray spectra. Usually, faint AGN X-ray spectra are fit by simple power-law models. The effect of increasing column density is that the soft part of the spectrum is suppressed more and more, i.e. the spectrum becomes harder at high $N_{\rm H}$. Many works in the field use an $N_{\rm H}$ value of 10^{22} cm^{-2} to distinguish between X-ray absorbed and unabsorbed objects. However, in practice it is not possible to determine $N_{\rm H}$ values for samples with typically very faint X-ray sources, due to the small number of observed photons. Therefore, one has to resort to hardness ratios measured from coarse X-ray bands. At high redshifts in general it gets more difficult to determine absorption values from X-ray spectral information, because the absorption cutoff is gradually shifting out of the observed band to lower energies. In particular, there are several claims in the literature that at high redshifts BLAGN tend to show significant absorption (see e.g. Brusa et al. 2007; Wang et al. 2007), but substantial systematic effects have to be taken into account here. First, $N_{\rm H}$ values can only be positive, so that the scatter in the data produces spurious absorption values even for perfectly unobscured objects (see e.g. the discussion in the appendix of Tozzi et al. 2006). Those spurious absorptions get larger with increasing redshift. Also, warm, ionised absorbers are present in many AGN, producing a deep trough in the X-ray spectrum around the oxygen edge (~0.5 keV), with a continuum recovering at softer energies. If the redshift of the object is such that the rest frame soft X-ray emission is shifted out of the observed band, these ionised absorbers can easily be mistaken for intrinsic cold gas absorption. This is in particular true for high-redshift broad absorption line (BAL) quasars (see e.g. Hasinger et al. 2002).

To overcome the difficulties of classification in either the optical or the X-ray bands, a combined optical/X-ray classification scheme has been introduced (Schmidt et al. 1998; Szokoly et al. 2004; Zheng et al. 2004). It first involves a threshold X-ray luminosity, which is set at $\log(L_{\rm X}) > 42$ erg s^{-1} to differentiate against the most luminous star-forming galaxies. All point-like X-ray sources with higher luminosities are considered as AGN. The second parameter is the X-ray hardness ratio HR, defined as

$$HR = (H - S)/(H + S), \quad (1)$$

with S and H the count rates in the soft and hard bands, respectively. This is illustrated in Fig. 2, which shows the observed hardness ratios as a function of redshift for objects selected from *XMM-Newton* and Chandra surveys with high-quality optical spectroscopy and well-determined hardness ratios. The differences in the response curves of the different *XMM-Newton* and Chandra surveys are small enough ($\Delta HR \sim 0.1$) that they do not significantly distort the observed hardness ratio distributions. The left part of the figure shows objects spectroscopically classified as broad-line AGN (BLAGN), while the right part shows AGN without broad emission lines. The BLAGN show a very narrow range of hardness ratios, independent of redshift. The

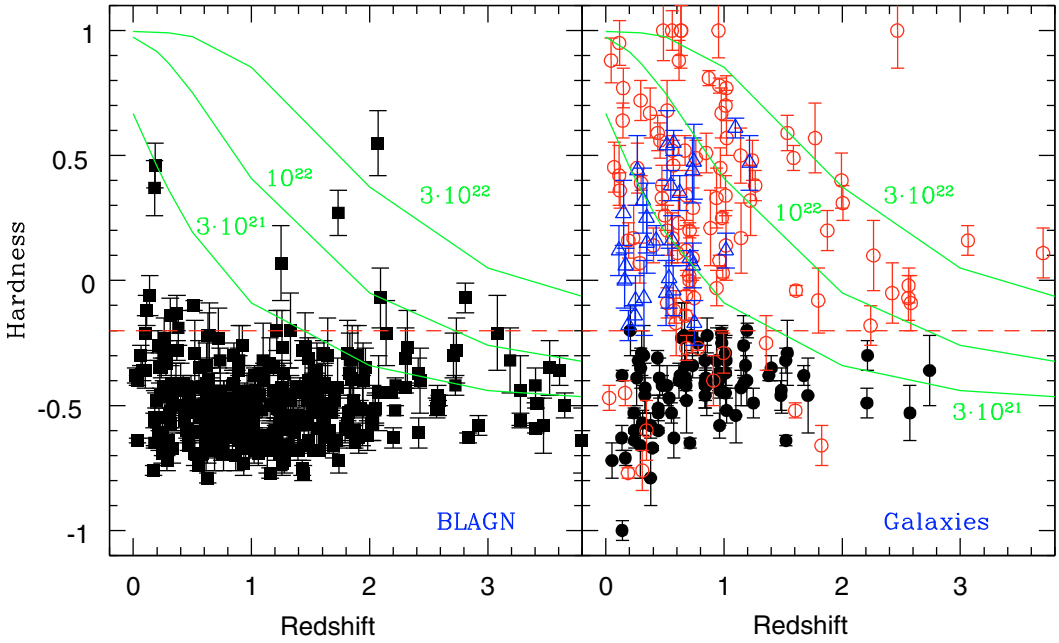

Fig. 2. The hardness ratio of X-ray sources selected from *XMM-Newton* and *Chandra* surveys with reliable optical spectroscopic classification and hardness ratio errors less equal than 0.15 as a function of redshift. *Left*: 320 objects optically classified as broad-line AGN (BLAGN). *Right*: objects without broad lines in their optical spectra. Sources classified as type-1 AGN by their X-ray hardness ratios (109 objects) are indicated by filled circles, spectroscopically classified type-2 AGN (200 objects) by open circles and objects spectroscopically classified as normal galaxies by green triangles (140 objects). The green solid lines in both diagrams are model predictions for a grid of power-law AGN spectra with photon index 2, locally absorbed through different column densities, as indicated in the plot.

reason for this is that BLAGN are strongly dominated by unabsorbed, powerlaw-type X-ray spectra, which do not change shape when they are redshifted. Only 11 out of 320 objects in this sample (3.4%) have *HR* values higher than −0.2, which can therefore conveniently be used as a threshold that distinguishes between X-ray absorbed and unabsorbed objects. BAL QSO are treated as BLAGN in this context. They are among the most absorbed BLAGN. In contrast, the non-BLAGN show hardness ratios spread out over a much wider range. In particular there is a kind of bimodal distribution, about half of the objects have *HR* values smaller than −0.2, consistent with unabsorbed spectra, and the rest have higher hardness ratios. There is also a clear trend of decreasing hardness ratios with redshift, which is because at higher redshifts the exponential low-energy cutoff in the X-ray spectra of absorbed sources is shifting towards lower energies. The latter effect leads to a degeneracy between absorbed and unabsorbed X-ray sources at high redshifts, which can no longer be distinguished using their hardness ratios.

Given this information, both the optical and X-ray selection effects and systematic errors in the distinction between absorbed and unabsorbed sources can be largely overcome by combining optical and X-ray spectral diagnostics. For those sources, which are unambiguously classified either as BLAGN or as NLAGN, using their optical/NIR spectra, the optical type-1/type-2 classification is maintained. For simplicity, Seyfert subclasses up to Sy1.5 (i.e. 1.2, 1.4, and 1.5) are sorted into the type-1 class, while subclasses above the Sy1.5 (i.e. 1.8, 1.9) are sorted into the type-2 class. Sources, for which optical spectroscopy does not allow an unambiguous distinction between type-1 and type-2 are classified by their hardness ratios. An AGN with a hardness ratio $HR < -0.2$ is called type-1, and with $HR > -0.2$ type-2. This classification also has the advantage that it can be applied for sources with no spectroscopic information, but which have reliable photometric redshifts. The other advantage is its relation to a simple measurable quantity, the hardness ratio that can in principle be included in models of the X-ray background. In addition, there are obvious systematic effects and difficulties. A small fraction of AGN are known not to follow the simple optical/X-ray obscuration/absorption correlation, either broad-line AGN have absorbed X-ray spectra (e.g. for BAL QSOs, see e.g. Hasinger et al. 2002; Chartas et al. 2002) or narrow-line AGN apparently have unabsorbed X-ray spectra (see e.g. Panessa & Bassani 2002). Also, as shown in Fig. 2, the hardness ratio threshold corresponds to different $N_{\rm H}$-values as a function of redshift. Finally, the dust obscuration affecting the optical properties of AGN versus gas absorption affecting the X-rays may be different, depending on environment and redshift. Nevertheless, these systematic effects are arguably far weaker than those of any of the other classifications individually. It is important to reiterate that the threshold hardness ratio of −0.2 used here is calibrated against the optical distinction between BLAGN and non-BLAGN and therefore corresponds to a somewhat lower NH value ($\sim 3\times10^{21}$ cm^{-2}) than typically used in the literature.

Figure 3 shows the AGN sample utilised in this study in the optical magnitude-X-ray flux and the redshift-luminosity plane, respectively. In principle, it would be possible to calculate emitted restframe luminosities from the known redshift and an absorption column density estimated from the hardness ratios for each object separately. However, that there are so few source photons detected for most objects in this sample introduces significant statistical errors into the results. Systematic biases are introduced into the analysis by the positive bound on the N_H values. Throughout this paper, therefore, only observed luminosities in the observed 2–10 keV band are used. The effects of intrinsic restframe luminosities can always be estimated using a forward modelling technique like e.g. in the GCH07 population synthesis model.

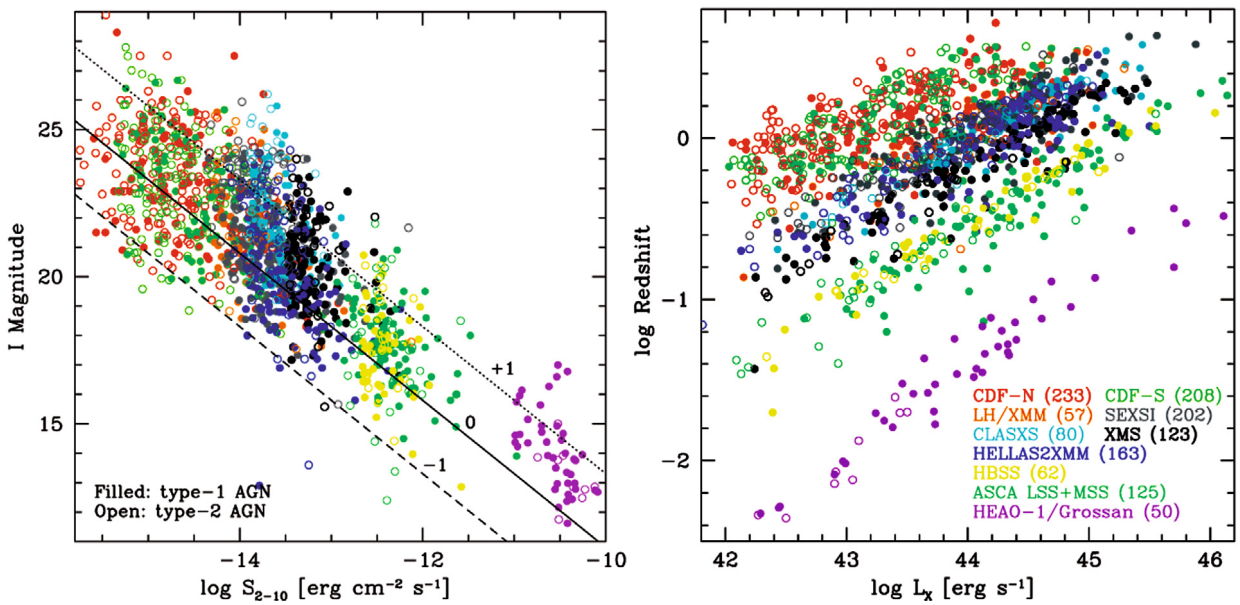

Fig. 3. *Left*: hard X-ray (2–10 keV) sample of 1290 AGN in the I-magnitude / 2–10 keV flux plane. The dotted, solid, and dashed diagonal lines indicate constant X-ray to optical flux ratios of $\log(f_X/f_{opt}) = -1, 0$, and $+1$, respectively. Filled symbols refer to type-1, and open circles to type-2 AGN as defined in Sect. 3. *Right*: the same data in the redshift / luminosity plane. Luminosity here and throughout the paper refers to the observed luminosity, i.e. uncorrected for intrinsic absorption.

4. Number counts of different populations

The combination of several surveys with a wide range of sensitivity limits and solid angle coverage provides a unique resource. On one hand, the surveys presented here resolve a large fraction of the 2–10 keV X-ray background. On the other, we have an almost complete optical identification and redshift determination for all components. We are thus in a position to study the contribution of different object classes to the X-ray background. Using the solid angle versus flux limit curve given in Fig. 1 the number counts for different classes of sources were constructed. Figure 4 gives the cumulative source counts normalised to a Euclidean behaviour: $N(>S_{2-10})\,S_{X14}^{1.5}$, where S_{X14} is the 2–10 keV flux in units of 10^{-14} erg cm^{-2} s^{-1}. A Euclidean relation would be a horizontal line in this graph. Separate curves are shown for the total sample, the type-1 and type-2 AGN, as well as for galaxies. The total and the AGN source counts display the well-known deviation from a Euclidean behaviour at low fluxes. For each of these populations a smoothly broken power-law was fit to the differential source counts:

$$N(S) = (\,(NS_{X14}^{\gamma 1})^{-1} + ((N/S_b^{\gamma 2-\gamma 1}S_{X14}^{\gamma 2})^{-1}\,)^{-1}. \quad (2)$$

The best-fit parameters for those are given in Table 4. As predicted in the GCH07 population synthesis model, type-1 AGN dominate at high fluxes, while type-2 AGN start to dominate at fluxes below 10^{-14} erg cm^{-2} s^{-1}. There is, however, a significant difference between the observed number counts and the model prediction, which will be addressed later.

An earlier attempt to disentangle the contribution of the different source classes to the number counts has been done by Bauer et al. (2004; see also Brandt & Hasinger 2005). However, there are systematic differences in this analysis: the redshift incompleteness and the different classification schemes for absorbed and unabsorbed AGN make a direct comparison difficult. If we compare the surface densities for different classes of sources above a 2–10 keV flux of 2.5×10^{-16} erg cm^{-2} s^{-1}, close to the sensitivity limit of the deep Chandra surveys, a very good match is found for the total X-ray source population (~4400 deg^{-2} for both analyses). The type-1 AGN surface density derived in this analysis (~1330 deg^{-2}) is somewhat higher than the surface density of X-ray unabsorbed objects in

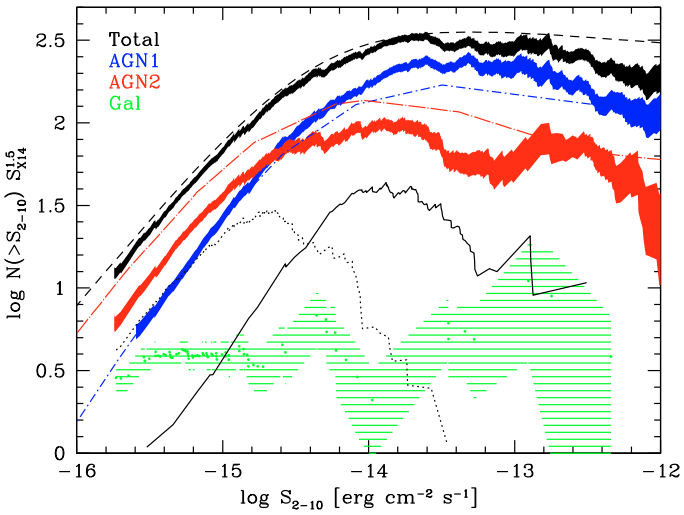

Fig. 4. Cumulative number counts for different subsamples of the data used here. For clarity the data have been normalised to a Euclidean slope ($N(>S)\cdot S_{X14}^{1.5}$). The upper black band shows the data points and 1σ errors for the total sample in comparison to the analytical description (black dashed line) from Moretti et al. (2003). The blue band shows the AGN type-1 number counts in comparison to the model prediction (blue dot-short-dashed line) by GCH07. The red band is for type-2 AGN, again in comparison to the Gilli et al. prediction (red dot-long-dashed line). The green band and corresponding data points show the number counts of galaxies (see text), which are consistent with a Euclidean behaviour down to the faintest fluxes. The thin solid line peaking in the middle of the flux range shows the number counts for the ~8% unidentified sources in the sample and the thin dotted line the counts of those sources with only photometric redshifts.

Table 4. Differential number counts best-fit parameters.

Sample	N [deg^{-2}]	γ_1	$S_b/10^{-14}$ [erg cm^{-2} s^{-1}]	γ_2	χ^2
Total	167.9 ± 15.6	2.64 ± 0.03	0.99 ± 0.15	1.24 ± 0.06	1.35
AGN1	122.2 ± 15.0	2.67 ± 0.03	1.39 ± 0.22	0.97 ± 0.08	1.36
AGN2	35.6 ± 3.5	2.62 ± 0.04	0.33 ± 0.06	0.82 ± 0.15	1.36

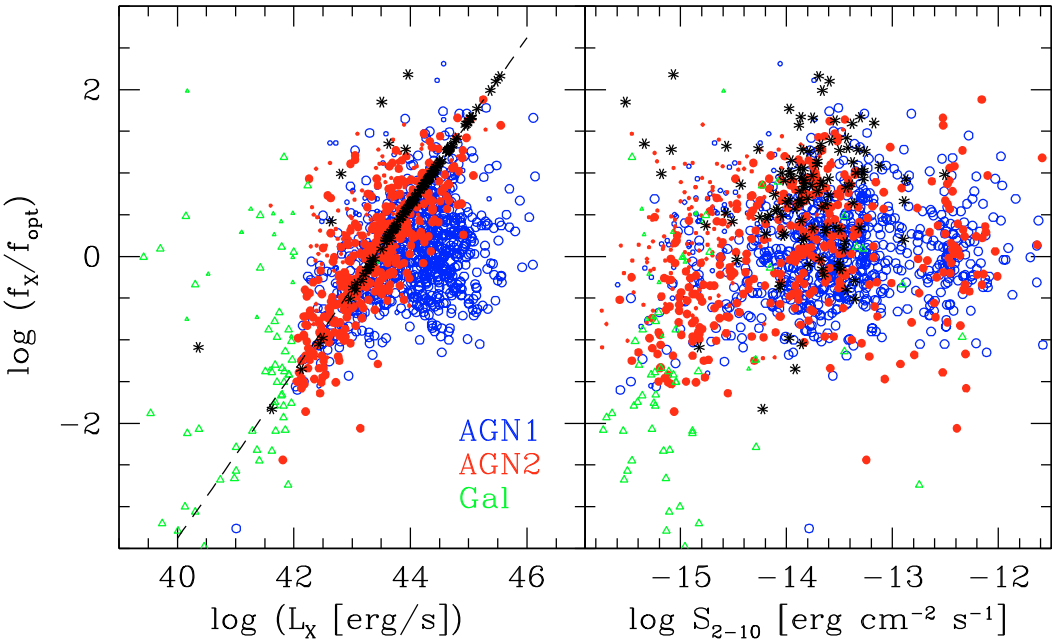

Fig. 5. The optical to X-ray flux ratios of the sample objects as a function of observed X-ray luminosity (*left*) and X-ray flux (*right*). Objects classified as type-1 AGN are shown by blue open circles, type-2 AGN as filled red circles, and galaxies as green triangles. Objects with spectroscopic redshift information are plotted with larger symbols and those, for which only photometric redshifts exist, with small symbols. The unidentified objects, for which crude redshifts have been assigned, are shown as black asterisks.

Bauer et al. (~780 deg^{-2}). On the other hand, the type-2 AGN surface density here is correspondingly lower (2250 deg^{-2} versus ~2900 deg^{-2}), respectively. Figure 4 also shows that galaxies, defined in this analysis as X-ray sources with luminosities lower than 10^{42} erg cm^{-2} s^{-1}, appear at the lowest fluxes and are consistent with Euclidean behaviour. Their space density at a flux of 2.5×10^{-16} erg cm^{-2} s^{-1} is ~840 deg^{-2}, compared to the range of 370–640 deg^{-2} observed by Bauer et al. The number counts of the galaxies defined in this way are about a factor of 3 higher than those predicted by Ranalli et al. (2003) for purely star-forming galaxies. This excess could indicate that the objects in this sample still have a substantial AGN contribution. Some of these X-ray sources could also be associated with diffuse emission in groups of galaxies. The figure also shows that the unidentified sources are conveniently situated at intermediate fluxes, so that they are unlikely to introduce a bias into the number counts. At fainter fluxes a larger proportion of objects are optically too faint for reliable spectroscopy, so that photometric redshifts have to be employed.

5. Correcting redshift incompleteness

As noted in Table 1, about 8% of the sample remains without redshift identification, compared to about 13% with only photometric redshifts. While this is a small fraction, the incompleteness most likely depends on redshift, so that systematic redshift and therefore spurious evolution effects may be introduced in the analysis. On the other hand, as Fig. 4 shows, the unidentified sources are mainly at intermediate fluxes. The reason is that they are typically from serendipitous *Chandra* and *XMM-Newton* surveys, where the quality of the optical photometry available does not allow a photometric redshift determination as accurately as in the deepest fields, which have excellent multi-band photometry.

It has been shown by Fiore et al. (2003) that for objects, where the optical light is dominated by their host galaxy (i.e. non broad-line AGN), there exists a correlation between X-ray luminosity and the optical to X-ray flux ratio f_x/f_{opt}. This is probably due mainly to the rather limited range of AGN host galaxy absolute luminosities, while AGN luminosities can occupy a much wider range. To test this conjecture for the AGN sample utilised here, the f_x/f_{opt} ratios are plotted against luminosity and X-ray flux in Fig. 5. As is well known, the X-ray sources show a substantial scatter in their X-ray to optical properties. However, unlike type-1 AGN, which at high luminosity are dominated by their non-thermal energy output both in the optical and X-ray regimes, type-2 AGN indeed show a significant trend toward higher X-ray/optical flux ratios with increasing redshift. This correlation could be fit by a simple proportionality between X-ray luminosity and X-ray to optical flux ratio:

$$\log(L_X) = \log(f_X/f_{opt}) + 44.38. \quad (3)$$

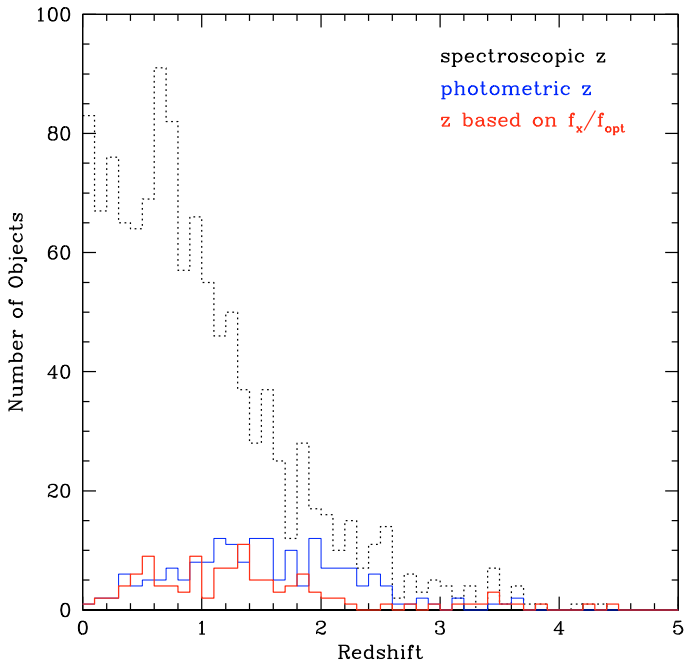

Fig. 6. Redshift distribution of objects with high-quality spectroscopic redshifts (thick black histogram), with photometric redshifts (thin blue histogram) and with crude redshifts estimated using the X-ray to optical flux ratios (dashed red histogram).

Table 5. Type-2 fraction as a function of luminosity, measured in the redshift interval z = 0.2–3.2.

Lmin	Lmax	t1′	t2′	t2′/(t1′+t2′)	t1	t2	t2/(t1+t2)
42.0	42.2	4	18	0.82 ± 0.08	5	18	0.78 ± 0.08
42.2	42.5	8	40	0.83 ± 0.05	9	40	0.82 ± 0.06
42.5	42.7	24	38	0.61 ± 0.06	24	39	0.63 ± 0.06
42.7	43.0	25	52	0.68 ± 0.05	26	53	0.67 ± 0.05
43.0	43.2	38	40	0.51 ± 0.06	41	42	0.51 ± 0.06
43.2	43.5	48	52	0.52 ± 0.05	54	53	0.50 ± 0.05
43.5	43.7	58	65	0.53 ± 0.05	65	72	0.53 ± 0.04
43.7	44.0	71	54	0.43 ± 0.04	71	64	0.47 ± 0.04
44.0	44.2	93	31	0.25 ± 0.04	103	41	0.28 ± 0.04
44.2	44.5	121	20	0.14 ± 0.03	128	34	0.21 ± 0.03
44.5	44.7	88	14	0.14 ± 0.03	92	21	0.19 ± 0.04
44.7	45.0	58	12	0.17 ± 0.05	58	17	0.23 ± 0.05
45.0	45.2	25	3	0.11 ± 0.06	26	6	0.19 ± 0.07
45.2	45.5	16	1	0.06 ± 0.06	16	1	0.06 ± 0.06
45.5	46.2	13	1	0.07 ± 0.07	13	1	0.07 ± 0.07

Quantities t1′ and t2′ with primes refer to the sample ignoring the unidentified sources, while quantities t1, t2 without primes refer to the sample including crude redshifts for the unidentified sources.

The slope of this relation is the same as in the work of Fiore et al. (2003). For all objects without redshift information, a crude redshift was estimated using this relation, including the objects in the HELLAS2XMM survey, where crude redshifts have already been estimated with a similar method by Fiore et al. (2003) and Mignoli et al. (2004). Bauer et al. (2004) and Barger et al. (2005) have shown that the Fiore et al. relation breaks down for very faint optical counterparts ($R > 25$). Indeed, a few objects indicated with asterisks in Fig. 5, originating in the CDF-S and CDF-N surveys fall off the main correlation line because their optical counterparts are too faint. For these objects, statistically rather uncertain photometric redhifts have been utilised instead of the crude redshifts derived from the Fiore et al. relation.

Figure 6 shows the redshift distribution, separately for spectroscopic, photometric, and crude redshifts. It is reassuring that the distribution of the crude redshifts is very similar to that of the photometric redshifts. Given that the flux distribution of the unidentified sources peaks in the middle of the sample range, the crude redshifts will probably not bias the results. Although individually they have very low reliability, in a statistical treatment they should give a fair estimate of the systematic effects involved in the redshift incompleteness.

Since the AGN classification scheme discussed above, in the absence of optical spectroscopy can still differentiate between type-1 and type-2 AGN, it is also applied to the unidentified sources with crude redshifts in order to estimate luminosities and to study the effect of the incompleteness on the analysis below.

6. The fraction of absorbed AGN

6.1. Luminosity-dependence of type-2 fraction

A comparison of the AGN type-2 and type-1 in the right panel of Fig. 3 shows that there is a much larger fraction of type-2 AGN at lower luminosities. Indeed, this confirms what had been found previously by different teams. Ueda et al. (2003) studied the hard X-ray luminosity functions of ~230 AGN, based largely on *ASCA* and deep *Chandra* surveys, with about 95% completeness. They found that the fraction of type-2 AGN decreases with X-ray luminosity, $L_{2-10\,\mathrm{keV}}$. Similar results have been obtained independently from different samples by Steffen et al. (2003) and Hasinger (2004) and later by La Franca et al. (2005). Treister & Urry (2005) and GCH07 have included such luminosity-dependent absorption trends in their population synthesis models.

To demonstrate the trend observed in the sample studied here, the type-2 fraction (i.e. the number of type-2 AGN divided by the total number of AGN in any particular subsample) was first calculated as a function of X-ray luminosity. In order to minimise possible redshift effects, the analysis was carried out in the redshift range $0.2 \le z \le 3.2$, which was chosen for simplicity to be compatible with the redshift shells used in the later analysis and to minimise any systematic effects that could happen at the lowest and highest redshifts. The results are shown in Table 5 and Fig. 7 (left). To keep track of the systematic selection effects introduced by the unidentified sources, the calculation was performed separately for the sample ignoring the unidentified sources and for that with crude redshifts included. Because the individual subsamples of type-1 and type-2 AGN sometimes contain small numbers, for which Gaussian statistics do not apply, the Gaussian equivalent error bars of the type-2 fraction were computed following Gehrels (1986): $\Delta N = \sqrt{N + 0.75}$.

Figure 7 (left) shows the trend toward a decreasing absorption fraction with increasing X-ray luminosity with unprecedented accuracy. This figure also demonstrates that the redshift incompleteness effects are moderate and mainly affect objects at higher luminosity. A simple linear function has been fit to the completeness-corrected data points. It yields a slope of -0.226 ± 0.014 and a marginally acceptable reduced χ^2 of 1.96. A flattening of the decline is expected at the highest luminosities, because the simple linear fit does not preclude negative values. A comparison of this new data with other results in the literature is made in Sect. 7.

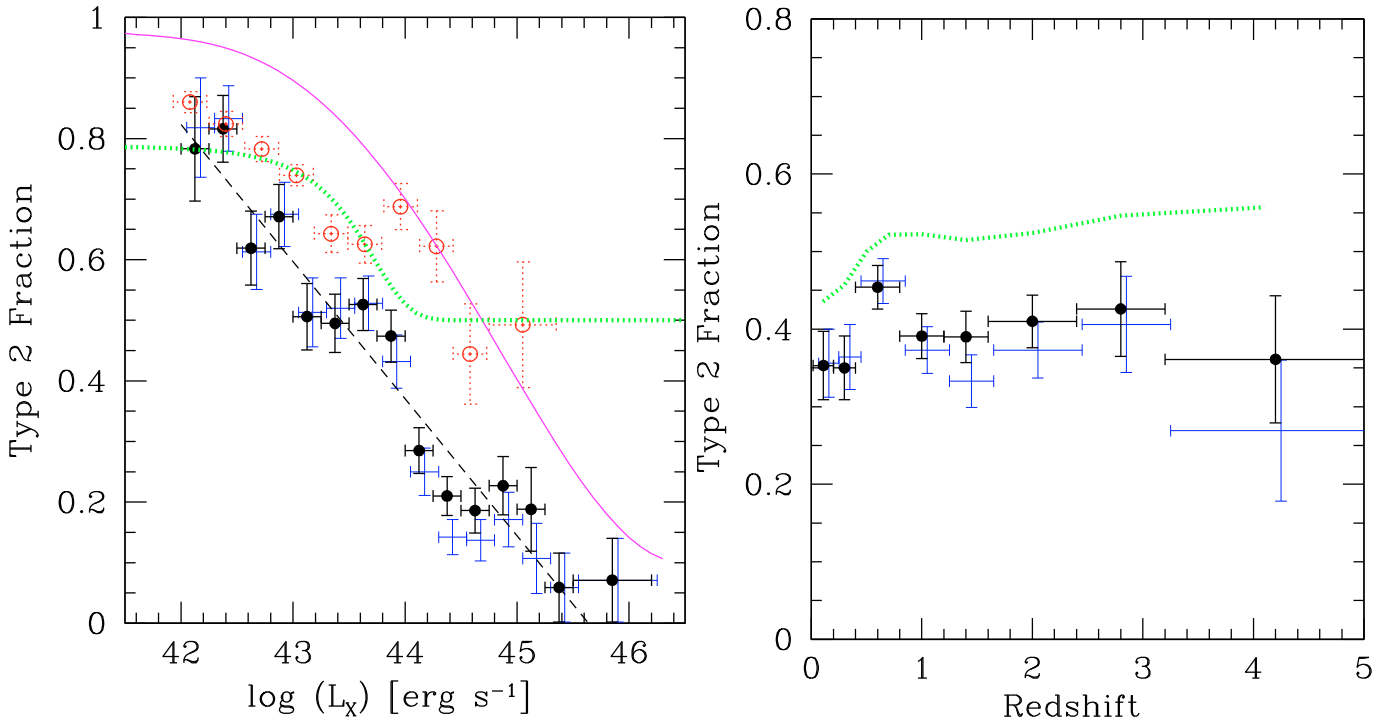

Fig. 7. *Left*: type-2 fraction as a function of luminosity, based on the data in the redshift range z = 0.2–3.2. The thin blue data points show the sample ignoring the unidentified sources, while the thick black data points with filled circles include the crude redshifts derived in Sect. 5. For clarity the thin blue points are shifted slightly to higher luminosity. A simple linear function fit to the black data points is shown as a dashed black line. The data points with red circles are derived using optical line widths of a sample of [OIII] selected AGN from the SDSS (Simpson 2005). The solid magenta line is from silicate dust studies of a sample of AGN observed with Spitzer in the MIR (Maiolino et al. 2007). The MIR data points of Treister et al. (2008, not shown here) are fully consistent with the Maiolino curve. The dotted green line shows the ratio of Compton-thin absorbed AGN to all Compton-thin AGN assumed in the GCH07 population synthesis model. *Right*: the observed fraction of type-2 AGN as a function of redshift. The colour coding of the thin blue and thick black data points is the same as in the left figure. The green solid line shows the prediction of the GCH07 model, assuming no redshift evolution in the absorbed fraction and folding over the solid angle sensitivity curve from Fig. 1. The error bars along the Y-axis in this and later figures all give 1σ uncertainties.

6.2. Redshift-dependence of AGN type-2 fraction

To address a possible evolution of the obscuration fraction with redshift, one can first simply determine the observed ratio of type-2 versus total AGN, integrated over all luminosities, in shells of increasing redshift. This is very similar to what was done by Treister & Urry (2006). Figure 7 (right) shows the dependence of the observed fraction of absorbed sources on redshift. To first order this data indicates a flat behaviour, apart from a small increase at redshifts below z = 0.8. The diagram also shows the type-2 fraction as a function of redshift predicted for the current sample from the most recent background synthesis model (GCH07), which assumes no evolution in the absorbed fraction. This curve shows that the small rise in the observed type-2 fraction at the lowest redshifts can be understood as an effect of the different flux limits for type-1 and type-2 sources in each survey (the last ones are harder to find because of absorption). The comparison with this model and with the Treister & Urry data points will be discussed in Sect. 7.

Figure 7 (right) is integrated over all luminosities in each redshift shell and is therefore possibly hiding trends, which might be observable in a better resolved parameter space. For a better diagnostic of the redshift evolution of the type-2 fraction, the dependence of the type-2 fraction on luminosity was analysed separately in different redshift shells. In Fig. 8 the same trend toward a decreasing absorption fraction as a function of X-ray luminosity, as observed in the total sample (see Fig. 7 left) is confirmed in each individual redshift shell. The same linear trend has been fit to the data points in each individual panel. First both the normalisation of the curve at $\log(L_X) = 43.75$ and the slope of the relation have been left as free parameters in the individual fits. The last column of Table 6 shows the slopes derived for the individual fits. Since they are all consistent with one another, the average slope over all panels has been determined to -0.281 ± 0.016. This slope is somewhat steeper than that derived for the total sample in the redshift range 0.2–3.2 (see above), which is a consequence of the increasing absorbed fraction with redshift.

The data in the individual panels were then again fit with a linear relation, but this time keeping the slope fixed to the average value of −0.281. The results of these fits are shown in Fig. 8 and also in Table 6. For every redshift shell this table shows the norm of the linear fit to the luminosity-dependence in Col. (2), taken at a value of $\log(L_X) = 43.75$ in the middle of the range. There is a clear trend toward an increasing normalisation of the absorbed fraction with redshift, which can be seen in the comparison in Fig. 8 and in the corresponding data in the table. However, to quantitatively estimate the evolution of the absorbed fraction with redshift, the systematic selection effects have to be corrected for. They stem from how in every flux-limited sample it is harder to detect absorbed objects compared to unabsorbed ones of the same intrinsic flux. Folding this selection effect over the solid angle as a function of flux limit of the current metasample, one can in principle obtain a correction curve as a function of redshift. For simplicity, here the green curve in Fig. 7 (right) determined for the GCH07 model folded with the effective solid

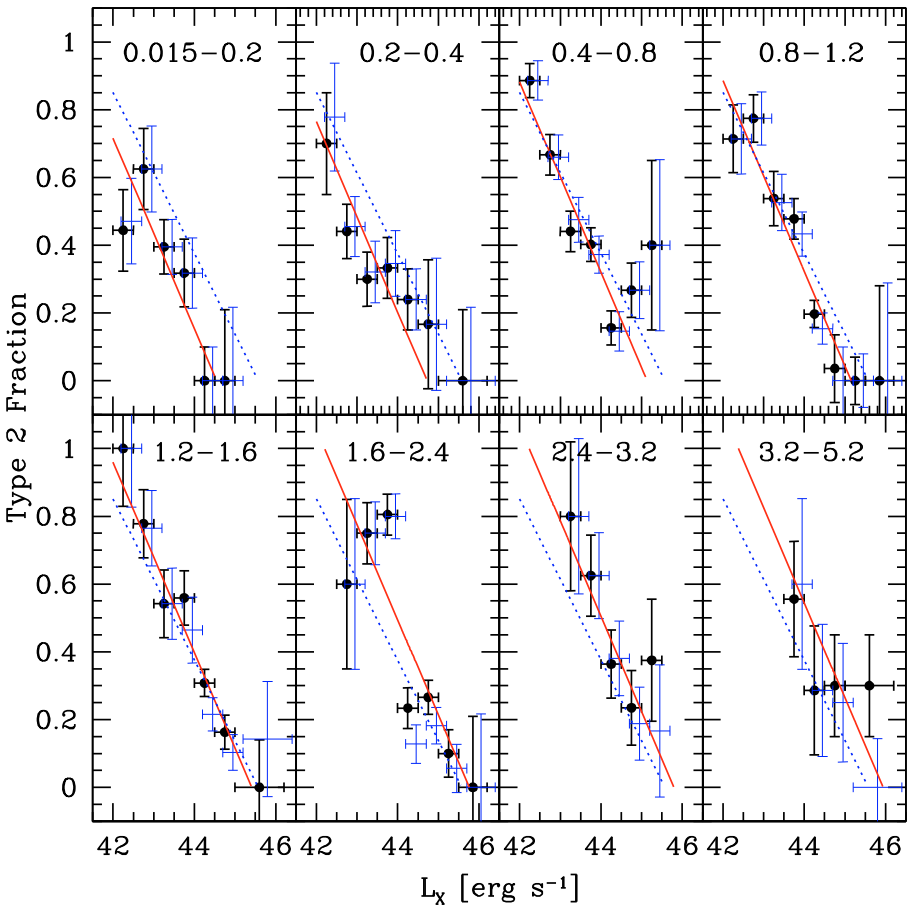

Fig. 8. Variation in the type 2 fraction with luminosity for different redshift shells. The thin blue data points show the sample ignoring the unidentified sources, while the thick black data points with filled circles include the crude redshifts derived in Sect. 5. The dotted blue line gives the fit to the average relation in the redshift range 0.2–3.2.

angle sensitivity curve in Fig. 1 and normalised to a redshift of 2 was used. The (small) correction values are given in Col. (3) of Table 6. With this correction applied, finally the corrected normalisation can be calculated for every redshift shell, which is given as Col. (4) of Table 6.

This corrected normalisation has been plotted as a function of redshift in Fig. 9. A significant increase in the absorbed fraction norm with redshift is seen from this figure. This increase, however, seems to saturate above a redshift of $z \sim 2$. Therefore, a broken power-law was fit to the data: $t_2(z) = t_2(0) \cdot (1+z)^{\alpha_1}$ for $z \le z_b$, saturating at $t_2(z) = t_2(z_b)$ for $z > z_b$. The best-fit parameters are determined to $t_2(0) = 0.279 \pm 0.024$, $\alpha_1 = 0.62 \pm 0.11$, $z_b = 2.06 \pm 0.47$, and the reduced χ^2 of this fit is 0.82. The evolution in the absorbed fraction in the redshift range up to $z \sim 2$ is therefore confirmed with a statistical significance of 5.7σ. To assess the significance of the apparent evolution saturation at high redshifts and to compare with previous works, a simple power-law $t_2(z) = t_2(0) \cdot (1+z)^{\alpha_2}$ was fit to the whole redshift range. The best-fit parameters for this representation are $t_2(0) = 0.308 \pm 0.022$ and $\alpha_2 = 0.48 \pm 0.08$ (i.e. a significance of 6.1σ). With a reduced χ^2 of 1.30, this fit is worse than for the broken power-law model but still marginally acceptable. Finally, a constant value can be ruled out with very high confidence (reduced $\chi^2 = 6.37$).

A simple power-law $t_2(z) = t_2(0) \cdot (1+z)^{\alpha_3}$ was also fit to the data without including the crude redshifts. The best-fit parameters for this data set are $t_2(0) = 0.309 \pm 0.024$ and $\alpha_3 = 0.38 \pm 0.09$ (a significance of 4.4σ) with a reduced χ^2 of 1.08. Including the crude redshift thus amplifies the evolution in the redshift range up to $z = 2$ and provides evidence for a saturation of this evolution. To assess the significance of this saturation it is useful to note the actual numbers of objects in the last two redshift bins, both including and excluding the crude redshifts. The redshift bin $2.4 < z \le 3.2$ contains 39 (38) type-1 and 29 (26) type-2 AGN (numbers in brackets refer to the sample without crude redshifts). The redshift bin $3.2 < z \le 5.2$ contains 23 (19) type-1 AGN and 13 (7) type-2 AGN. Including crude redshifts thus mostly affects the highest redshift bin.

7. Discussion

7.1. Systematic effects of different AGN classification schemes

In Sect. 3 different classification techniques for X-ray selected AGN were discussed. In most classical treatments, type-1 AGN are just defined by the presence of broad permitted lines observed in their optical spectra (see e.g. Steffen et al. 2003; Barger et al. 2005; Treister & Urry 2006). To estimate the systematic differences with the combined optical/X-ray classification employed in this paper, the luminosity- and redshift dependence of the type-2 fraction was recomputed for the sample using the same BLAGN classification scheme. In this case type-1 AGN are spectroscopically identified objects with broad emission

Table 6. Type-2 fraction norm in redshift intervals.

z Range	Norm	corr	corr. Norm	Slope
0.015–0.2	0.224 ± 0.045	0.83	0.269 ± 0.054	−0.25 ± 0.06
0.2–0.4	0.273 ± 0.041	0.87	0.313 ± 0.047	−0.16 ± 0.05
0.4–0.8	0.390 ± 0.025	0.95	0.409 ± 0.026	−0.28 ± 0.03
0.8–1.2	0.394 ± 0.027	1.00	0.396 ± 0.027	−0.29 ± 0.03
1.2–1.6	0.468 ± 0.030	0.98	0.476 ± 0.031	−0.30 ± 0.04
1.6–2.4	0.564 ± 0.030	1.00	0.565 ± 0.030	−0.36 ± 0.05
2.4–3.2	0.575 ± 0.060	1.04	0.551 ± 0.058	−0.27 ± 0.11
3.2–5.2	0.615 ± 0.086	1.06	0.578 ± 0.081	−0.11 ± 0.12

lines, while type-2 AGN are all other spectroscopically identified objects. For consistency with other works, objects with only photometric or crude redshifts are ignored here. Figure 10 shows the results of this analysis in comparison to the combined X-ray/optical classification and to the raw X-ray data from Treister & Urry (2006) and Treister et al. (2008). The left panel shows the observed dependence of the type-2 fraction on X-ray luminosity. The data points derived from the BLAGN only classification are fully consistent with the X-ray data from Treister et al. (2008), but at lower X-ray luminosities both are significantly higher than those from the combined X-ray/optical classification used here. This is mainly due to the large number of unabsorbed AGN at low to intermediate luminosities, missing in the BLAGN sample presumably due to dilution from the host galaxy light (see Fig. 2). The same trend is also seen in the right panel of Fig. 10, which shows a significant difference in the redshift dependence of the absorbed fractions determined by the two different methods.

7.2. Luminosity dependence of absorbed fraction

All analyses represented in Fig. 7 (left) based on X-ray and optical samples agree that there is a strong decline of the absorbed fraction with AGN luminosity. The X-ray analysis presented here confirms this trend in much more detail and with better statistical and systematic errors than previous X-ray analyses. Similar trends are found in other wavebands. Local Seyfert galaxies selected from the SDSS spectroscopy sample using the [OIII] lines show a fraction of BLAGN increasing with the luminosity of the isotropically emitted [O III] narrow emission line (Simpson 2005). To convert the [O III] line luminosity into a 2–10 keV luminosity for the display in Fig. 7, the empirical luminosity-dependent correlations found by Netzer et al. (2006) for type-1 and type-2 Seyfert galaxies were averaged as

$$\log \frac{L_{[\mathrm{OIII}]}}{L_{2-10}} = 13.7 - 0.358 \log L_{2-10}. \quad (4)$$

Mid-infrared (MIR) Spitzer low-resolution spectra of 25 luminous QSOS at redshifts between 2 and 3.5, combined with low-luminosity type-1 AGN, confirm this picture (Maiolino et al. 2007). These authors find a strong, nonlinear decrease (a factor of ten) in the thermal continuum dust emission at 6.7 μm with increasing 5100 Å optical continuum emission and [OIII]5007 line luminosity. They interpret this as a decreasing covering factor of circumnuclear dust as a function of luminosity. They clearly detect silicate dust emission features (see also Sturm et al. 2006), whose strength correlates with luminosity, accretion rate L/L_{Edd} and black hole mass M_{BH}.

Independently, Treister et al. (2008) have recently measured this covering fraction by studying the ratio of the MIR to bolometric luminosity in a sample of $z \sim 1$ BLAGN selected optically in the Sloan Digital Sky Survey (SDSS), the Great Observatories Origins Deep Survey (GOODS), and the Cosmic Evolution Survey (COSMOS). They use the Spitzer 24μ flux as a proxy of the MIR dust-reprocessed radiation. For their redshift range, this corresponds to ∼12μ, which according to Maiolino et al. (2007) and Sturm et al. (2005) is affected by the silicate emission and caused less by the reprocessed thermal dust emission. To estimate the bolometric luminosity of their AGN (primarily the blue bump) they use the Galex NUV data, sampling the rest frame waveband 875–1400 Å, which can possibly be affected by absorption from the Ly-forest and the dust extinction. Nevertheless, their results match the Maiolino et al. curve in Fig. 7 (left) almost perfectly.

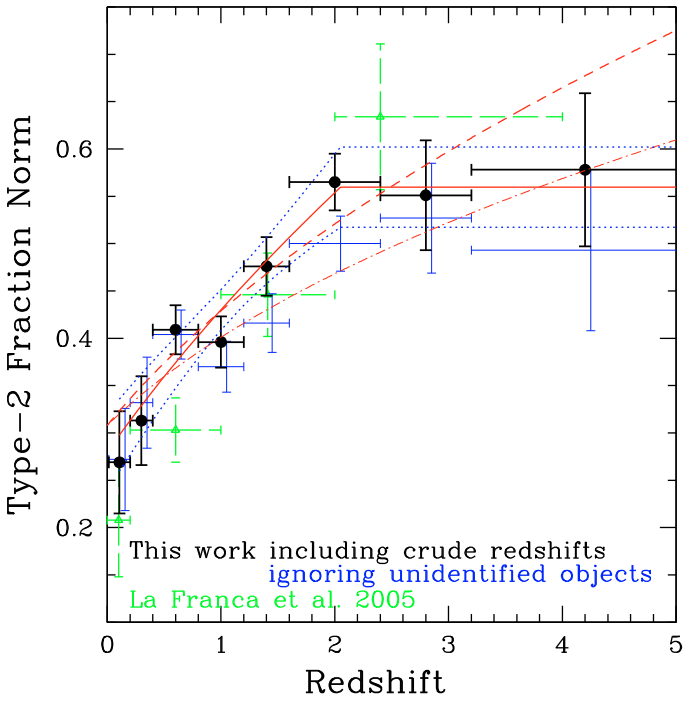

Fig. 9. Dependence of the normalisation of the type-2 fraction at $\log(L_{\mathrm{X}}) = 43.75$ with redshift (from the fits shown in Fig. 8). The red solid curve shows a saturated power-law fit to the solid black data (see text). The blue dotted lines give the 90% confidence intervals for this fit. The dashed red line shows a single power-law fit to the black solid data over the full redshift range, while the dot-dashed line shows the same single power-law fit to the thin blue data points without including the crude redshifts. The dashed green data points are from La Franca et al. (2005).

Of course, all the sample selections represented in Fig. 7 (left) are subject to systematic errors and selection biases. The X-ray surveys in the 2–10 keV band almost completely miss the population of Compton-thick Seyfert galaxies, which are barely detectable only above 10 keV (see e.g. GCH07). However, first significant minority samples of Compton-thick candidate objects have been detected in deep-wide X-ray surveys (Tozzi et al. 2006; Hasinger et al. 2007; Brunner et al. 2008), consistent with the GCH07 model predictions. Including information from deep MIR surveys, there is now convincing evidence that the population of Compton-thick intermediate-luminosity AGN even at higher redshifts is of the same order as that of Compton-thin AGN (see e.g. the recent results in the CDFS by Daddi et al. 2007 and Fiore et al. 2008a as well as in the COSMOS field by Fiore et al. 2008b). Using a combination of mid-infrared and optical spectroscopy in comparison to their X-ray properties, Alexander et al. (2008) identified seven Compton-thick high-luminosity AGN at redshifts $z \sim$ 2–2.5 and

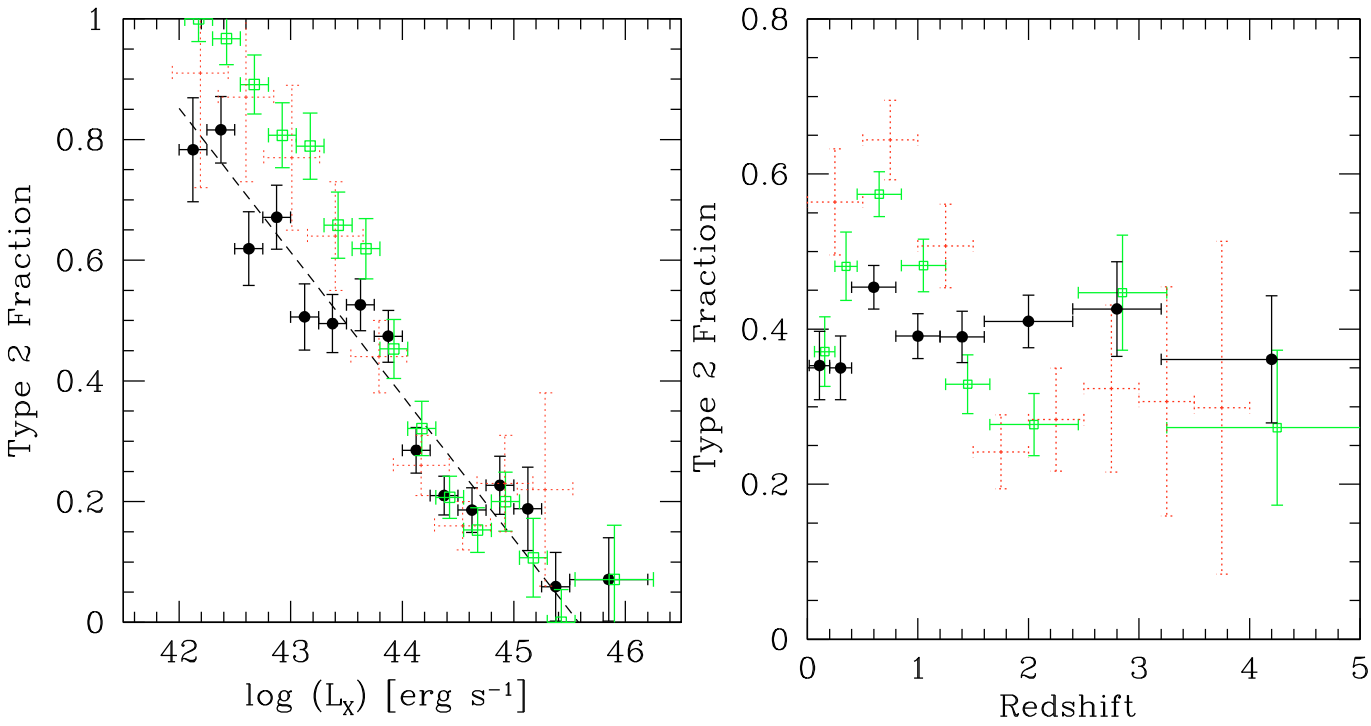

Fig. 10. Comparison of type-2 fractions as a function of luminosity (*left*) and a function of redshift (*right*) for different AGN classification schemes. The filled black data points with thick error bars correspond to the combined optical/X-ray classification introduced in Sect. 3 and are identical to those in Fig. 7. The green data points with open squares and thin error bars have been derived using a purely optical spectroscopic classification, where only BLAGN are classified as type-1 objects (see Fig. 2). Red data points with dotted error bars are from Treister et al. (2008; *left*) and from Treister & Urry (2006; *right*), respectively.

could show that their space density is as large as that of their unobscured counterparts. Optical surveys, on the other hand, while including many of the Compton-thick AGN missing in X-ray samples, fail on the AGN populations diluted by their host galaxy (see Fig. 2), and also those so heavily obscured that very little scattering or ionising radiation escapes (see e.g. Ueda et al. 2007). Nevertheless, the agreement of better than 20% between the optical sample selected from the SDSS using the [OIII] lines (Simpson 2005) and the hard X-ray selection from this paper is reassuring in this respect.

In Fig. 7 also the relation between absorbed Compton-thin AGN to all Compton-thin AGN assumed in the GCH07 X-ray background population synthesis model is shown. Because Compton-thick objects have been explicitly excluded in this curve, it can be directly compared to the observed 2–10 keV X-ray sample results. Please note, however, that this is the assumed intrinsic ratio, the real observations are still affected by additional selection effects. Nevertheless, it is apparent that this model overpredicts the fraction of obscured sources, in particular at high luminosities. This is also likely to be one of the reasons for the systematic difference between the predicted and observed number counts for type-1 and type-2 AGN in Fig. 4. Probably the best approximation of the true fraction of obscured objects is the Maiolino et al. relation. Hopefully, the GCH07 model can be updated accordingly in the future.

Physically, this luminosity-dependent fraction might be interpreted as a cleanout effect because more luminous AGN can dissociate, ionise, and finally blow away the dust in their environment. At face value this trend signals a breakdown in the simple unified AGN model, where the difference between type-1 and type-2 AGN is solely in the geometry of the observer's line of sight with respect to the absorber (Antonucci 1993). The luminosity dependence of the absorbed fraction indicates an intrinsic physical difference in the average absorber properties as a function of intrinsic AGN luminosity. The simplest interpretation of these findings is that low-luminosity AGN are surrounded by an absorbing/obscuring medium that covers a large solid angle (~80% of the sky as seen from the black hole), however, with an average column density much lower ($N_H \sim 10^{22}$ cm^{-2}) than the putative Compton-thick dusty torus of the unified model ($N_H \sim 10^{24-25}$ cm^{-2}). High-luminosity AGN are then able to clean out their environment, either by ionising the surrounding medium, or by blowing it away through an outflowing wind (see also Ballantyne, 2006; Müller & Hasinger 2007). This behaviour is also a key ingredient in the "blast wave AGN feedback" model presented recently by Menci et al. (2008), where AGN accretion luminosity, feedback, and absorption are intimately connected to one another.

7.3. Redshift dependence of absorbed fraction

The evolution of the luminosity-dependent obscuration fraction with redshift is still a matter of debate. A possible redshift dependence of the obscured fraction was reported by La Franca et al. (2005), using the HELLAS2XMM sample combined with other published catalogues, based on a total of 508 AGNs selected in the 2–10 keV band. On the other hand, other authors (e.g. Ueda et al. 2003, GCH07) have not found a significant redshift dependence. Using a population synthesis model for the X-ray background, Balantyne et al. (2006) predicted a type-2 AGN fraction that evolves as $(1+z)^{0.4}$. Treister and Urry (2006) have performed an analysis, using an AGN metasample of 2300 AGN with ~50% redshift completeness and find an increase in the type-2 AGN fraction proportional to $(1 + z)^{0.4}$. The differences between the

various results are very likely due to the different sample sizes and the ways, in which the redshift incompleteness, the different flux limits, and the AGN classification have been taken into account in the analysis.

The analysis in this paper shows a significant trend toward an increasing absorbed fraction with redshift. Interestingly, at first sight, the observed fraction of absorbed sources, has a redshift dependence very similar to the prediction of the no evolution GCH07 model (see Fig. 7, right) after correction for the identification incompleteness. This, however, turns out to be a "conspiracy" due to a combination of the shape of the luminosity- and redshift-dependence of the absorbed fraction. As can be seen in Fig. 3, the median of the sample shifts to higher luminosities at higher redshifts. In the case of the almost linear decrease in the absorbed fraction with luminosity observed in Fig. 7 (left) one would expect a significant decrease in the observed absorbed fraction if there was no redshift evolution (see also the model predictions in Fig. 2 of the Treister & Urry 2006 paper). This has to be compensated for by an increase in the absorbed fraction with redshift if an almost constant behaviour like the one in Fig. 7 (right) is observed. Alternatively, if at high luminosities the absorbed fraction is constant, as assumed in the GCH07 model, an almost constant trend with redshift is expected, assuming no evolution.

However, disentangling the data into separate redshift and luminosity intervals resolves the degeneracy of the analyses based on one-dimensional data sets. Figure 8 confirms with high statistical accuracy that the decreasing trend of the absorbed fraction with luminosity is present in all redshift intervals. A similar result has already been shown in broader redshift and luminosity bins by Barger et al. (2005); however, their results are affected by the systematic differences discussed in Sect. 7.1. Figure 8 also shows an increase in the absorbed fraction with redshift. If the data in each redshift slice are fit by a simple linear relation, the normalisation of this relation, here assumed for a luminosity $\log(L_X) = 43.75$ in the middle of the observed range, clearly shows an increase with redshift up to $z \sim 2$, where this trend seems to saturate. Figure 9 shows that this trend is highly significant and can be fit by a power-law evolution proportional to $(1+z)^{\alpha}$, with $\alpha = 0.62 \pm 0.11$. This evolution is thus substantially faster than the exponent $\alpha = 0.4 \pm 0.1$ originally found by Treister & Urry (2006). Several reasons can be envisaged for this difference. First, these authors have fit the power-law trend over the full redshift range, because the flattening of the curve was not apparent in their data. In addition they only used the BLAGN classification, which tends to over-estimate the absorbed fraction at low redshifts (see Fig. 10). Finally, the inclusion of crude redshifts in the analysis presented here tends to recover more absorbed objects at higher redshifts and higher luminosities.

Interestingly, the increase in the normalisation of the absorbed fraction relation with redshift is very similar to the observed fractions given in Fig. 6b of the La Franca et al. (2005) paper based mainly on the HELLAS2XMM sample (see also Fig. 9). This could, however, be somewhat of a chance coincidence, because their data show the observed ratios integrated over a broad luminosity range (more like Fig. 7, right, in this paper), and has its own systematic selection effects. Nevertheless, the trend originally claimed by La Franca et al. (2005) is fully confirmed here.

It is also interesting to note that the saturated absorption evolution found in this study shows a very similar redshift dependence to the space density evolution of the overall AGN population with an increase from zero redshift to a peak redshift, where the evolution is saturating. However, the absorption evolution is much shallower than the AGN density evolution.

7.4. Consequences for the broader context of AGN and galaxy co-evolution

The cosmological evolution of AGN in the X-ray, optical and radio wavebands can be described by a luminosity-dependent density evolution model, in which the peak of the AGN space density shifts to lower luminosities towards lower redshifts (see above and Hopkins et al. 2007). This evolutionary behaviour is very similar to the cosmic downsizing observed in the bolometric luminosity of the normal galaxy population (Cowie et al. 1996) and indicates that star formation and nuclear activity in galaxies go hand in hand. This kind of anti-hierarchical black hole growth scenario is not predicted by most semi-analytic AGN evolution models based on galaxy merger scenarios (e.g. Kauffmann & Haehnelt 2000; Wyithe & Loeb 2003; Croton et al. 2005; Menci et al. 2008; Rhook & Haehnelt 2008). Typically these models are able to explain the space density evolution of high-luminosity AGN, peaking at redshifts $z > 2$, but have difficulty matching the behaviour at lower luminosities. Some authors (e.g. Treister et al. 2004; Menci et al. 2008) attribute these differences to systematic selection biases against the identification of distant obscured, low-luminosity AGN, in particular if there is a strong evolution of absorption with redshift. The results of the analysis presented in this paper, although indeed confirming a significant evolution of obscuration, argue against this conjecture, because the evolution observed across the whole redshift range is too shallow (at most a factor of 2) to explain the dramatic luminosity-dependent density evolution effect. Therefore other ingredients are required to explain the observed AGN downsizing.

Important inputs to the solution of this puzzle may come from the study of colours and morphologies of the host galaxies of moderate-luminosity AGN at low to intermediate redshifts. The SDSS in combination with data from the Galaxy Evolution Explorer (GALEX) satellite are of help here. Kauffmann et al. (2007) analysed a volume-limited sample of massive bulge-dominated galaxies with data from both the SDSS and GALEX at redshifts $0.03 < z < 0.07$. The GALEX NUV data are a very sensitive indicator for low levels of star formation in these systems. These authors find that practically all AGN in their sample have rather blue NUV-r colours and the UV excess light is almost always associated with an extended blue disc, while galaxies with red outer regions almost never have a young bulge or a strong AGN. They suggest a scenario in which the gas of the outer disc is accreted onto the bulge-dominated galaxy over cosmic time and provides the mass reservoir to trigger sporadic AGN accretion and star formation through gravitational instabilities (see also Cavaliere & Vittorini 2000; Hammer et al. 2005). Interestingly, Schiminovich et al. (2007) show that in the NUV-r versus mass diagram, the local SDSS AGN are preferentially at high masses, but at colours in between the blue cloud and the red sequence, the so-called green valley (see also Fig. 11).

Similar results are found at higher redshifts from optical studies in deep and wide Chandra and *XMM-Newton* survey fields. Nandra et al. (2007) discuss the colour-luminosity diagram for AGN selected from the Chandra survey of the extended Groth strip in the redshift range $0.6 < z < 1.4$. They also find the AGN host galaxies in a distinct region of the colour-magnitude diagram, often in the green valley. They interpret this in the context of star formation quenching in massive galaxies, resulting in a migration from the blue cloud to

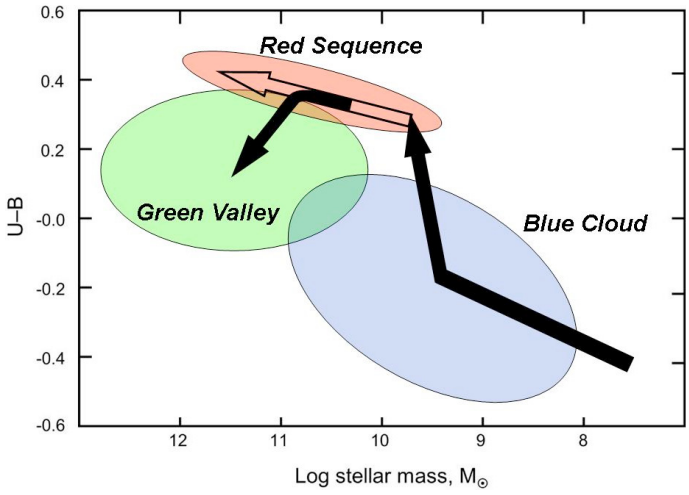

Fig. 11. Schematic arrows showing galaxies moving in the colour-mass diagram under different evolutionary assumptions (following Faber et al. 2007). It is conventionally assumed that galaxies on the red sequence are formed when two blue cloud galaxies merge with each other and the feedback from the growing central black hole is quenching star formation, leaving a dead and red bulge-dominated galaxy with a dormant supermassive black hole. Host galaxies of intermediate-luminosity AGN are often found in the region between the blue cloud and red sequence, the so-called green valley. The scenario described here tries to explain this by a re-juvenation of bulge-dominated galaxies through the accretion of fresh gas from their environment.

the red sequence. Silverman et al. (2008) present an analysis of 109 moderate-luminosity (log L_X < 42) AGN in the Extended Chandra Deep Field-South survey (Lehmer et al. 2000) with redshifts z = 0.4–1.1 and find a strong dependence of AGN host colours on the environment. Compared to all galaxies in the field they find that the fraction of galaxies hosting an AGN peaks in the green valley, in particular due to enhanced AGN activity in two narrow redshift spikes around z = 0.63 and z = 0.73 (see Gilli et al. 2005). They also find that AGN host galaxies in this redshift range typically have hybrid morpholgies between pure bulges and discs. They try to explain their findings in an AGN merger scenario, but remark that the merger-driven evolution timescales are typically too short to explain the abundance of green valley galaxies.

Putting these findings together, one arrives at a scenario possibly explaining the AGN cosmic downsizing as well as their colour and morphological evolution (see Fig. 11). In order to produce an AGN, we need two ingredients: a central supermassive black hole and efficient gas accretion. The fuel can either be provided by a major merger driving gas into the centre and simultaneously leading to an Eddington-limited growth of the black hole(s) (see e.g. Di Matteo et al. 2005; Li et al. 2006). In this case a bulge galaxy is formed and the feedback of the growing black hole can quench star formation. The result is a red bulge-dominated galaxy with a dormant supermassive black hole. The merger-driven evolution time scale is, however, rather short ($\sim 10^9$ years), so that only a small fraction of the galaxy population can be found in a transient state between the blue cloud and the red sequence. It is likely that the space density evolution of the most luminous QSOs, peaking in the redshift range z = 2–3, is a direct consequence of the merger history of massive halos. The results above show that there is also another source of gas supply, namely the accretion of fresh gas from the surrounding of a galaxy. In this way, a bulge-dominated galaxy with a central black hole that was formed during a previous merger event can be re-juvenated, leading to a disc surrounding the bulge. In the colour-mass diagram such a galaxy is therefore coming down from the red sequence into the green valley (see Fig. 11) and the galaxy assumes the hybrid bulge/disc morphology observed for the SDSS AGN and many of the X-ray selected intermediate-redshift AGN. The black hole can be fed through episodic star formation and accretion events, likely produced by gravitational instabilities in the outer disc. Since the black hole and the bulge have already been formed previously and the host galaxy is already relatively massive, the accretion typically happens at a rather low Eddington ratio, substantially smaller than in the merger case (see e.g. Marconi et al. 2004; Merloni & Heinz 2008). This mode of black hole growth is therefore slow enough that it can be observed in a large fraction of all galaxies, providing a natural explanation for the late evolution in the ubiquitous lower-luminosity AGN. This scenario is still rather descriptive and crude, but hopefully can be quantified by including the bimodal gas supply into semi-analytical evolution models in the future.

8. Conclusions

A metasample of hard X-ray selected AGN has been compiled from the literature, providing an unprecedented combination of statistical quality and spectroscopic along with photometric redshift completeness. Systematic differences in the selection of this rather heterogeneous set of samples were taken care of as far as possible and should not significantly bias the results. The small, but significant redshift incompleteness could be corrected for by using the correlation between luminosity and X-ray to optical flux ratio observed in non-broad-line AGN. A comparison between the analysis with and without including crude redshifts shows that the crude redshifts tend to enhance the high-redshift, high-luminosity bins, but the main results do not depend strongly on this choice.

The X-ray selected AGN could be classified using both optical spectroscopy and X-ray hardness ratios. This classification scheme appears more robust than either optical or X-ray classification alone. A strong decrease in the fraction of absorbed AGN was found with redshift. This trend confirms similar results obtained previously in the X-ray, but also optical and MIR bands. As expected, systematic selection effects are present between different bands, but do not dominate the results. This signals a break-down of the strong unified AGN model and indicates that high-luminosity AGN can clean out their environment.

The same decreasing trend with luminosity is found in all individual redshift shells up to $z \sim 3$. However, the data indicate a significant evolution of the absorbed AGN fraction, which increases by about a factor of 2 up to $z \sim 2$ and remains approximately constant thereafter. This rather shallow evolution implies that the luminosity-dependent AGN density evolution observed in the X-ray, optical, and radio bands is a real property of the parent population and not caused by systematic selection effects.

A new scenario is proposed in which the cosmic downsizing of the AGN population is due to two different fuelling mechanisms: on one hand, the efficient growth of luminous QSOs by galaxy mergers early in the universe; on the other the re-juvenation of pre-formed bulges and black holes by slow gas accretion over cosmic time.

Acknowledgements. I am indebted to Takamitsu Miyaji and Keisuke Shinozaki for providing the effective area curve, optical magnitudes, and identification details of the HEAO-1/Grossan sample. I also am grateful to Yoshihiro Ueda for providing me with the updated ASCA LSS and MSS hard X-ray samples and effective area curves. Marcella Brusa and Fabrizio Fiore helped me to obtain

some detailed unpublished information, e.g. X-ray hardness ratios and some new identifications for the HELLAS2XMM sample. I am particularly thankful to Peter Capak, who provided me with the unpublished photometric redshifts from his Ph.D. thesis for the CDF-N sources. I thank John Silverman, Vincenzo Mainieri, Jaqueline Bergeron, Peter Capak and Jeyhan Kartaltepe for permission to use unpublished redshifts in the CDF-S. I am grateful to Roberto Della Ceca for providing me with unpublished details of the HBSS sample. I thank Roberto Gilli, Andrea Comastri, Marcella Brusa, Fabrizio Fiore, Nico Capelluti, Roberto Maiolino, and Ezequiel Treister for very helpful discussions and in particular Roberto Gilli for providing the model prediction in Fig. 7 (right). Part of this work was supported by the German *Deutsche Forschungsgemeinschaft, DFG* Leibniz Prize (FKZ HA 1850/28–1). I thank the Institute for Astronomy, Manoa, Hawaii for the hospitality during my sabbatical visit in summer 2007, when a significant part of this work was done. This research has made extensive use of the NASA/IPAC Extragalactic Database (NED), which is operated by the Jet Propulsion Laboratory, California Institute of Technology, under contract with the National Aeronautics and Space Administration, as well as the SIMBAD database, operated at CDS, Strasbourg, France. This work has made use of observations carried out using the Very Large Telescope at the ESO Paranal Observatory under Programme ID(s): 170.A-0788, 074.A-0709, and 275.A-5060. I thank a competent referee and the language editor for very helpful and constructive comments, which helped to improve the paper.

References

Alexander, D. M., Bauer, F. E., Brandt, W. N., et al. 2003, AJ, 126, 539
Alexander, D. M., Chary, R. R., Pope, A., et al. 2008, ApJ, in press [arXiv:0803.0636]
Akiyama, M., Ohta, K., Yamada, T., et al. 2000, ApJ, 532, 700
Akiyama, M., Ueda, Y., Ohta, K., Takahshi, T., & Yamada, T. 2003, ApJS, 148, 275
Antonucci, R. 1993, ARA&A, 31, 473
Barcons, X., Carrera, F. J., Ceballos, M. J., et al. 2007, A&A, 476, 1191
Baldi, A., Molendi, S., Comastri, A., et al. 2002, ApJ, 564, 190
Ballantyne, D. R., Everett, J. E., & Murray, N. 2006, ApJ, 639, 740
Barger, A. J., Cowie, L. L., Bautz, M. W., et al. 2001, AJ, 122, 2177
Barger, A. J., Cowie, L. L., Capak, P., et al. 2003 AJ, 126, 632
Barger, A. J., Cowie, L. L., Mushotzky, R. F., et al. 2005, AJ, 129, 578
Bauer, F. E., Alexander, D. M., Brandt, W. N., et al. 2002, AJ, 123, 1163
Bauer, F. E., Alexander, D. M., Brandt, W. N., et al. 2004, AJ, 128, 2048
Brandt, W. N., & Hasinger, G. 2005, ARA&A, 43, 829
Bongiorno, A., Zamorani, G., Gavignaud, I., et al. 2007, A&A, 472, 443
Brunner, H., Cappelluti, N., Hasinger G., et al. 2008, A&A, 479, 283
Brusa, M., Comastri, A., Mignoli, M., et al. 2003, A&A, 409, 65
Brusa, M. et al. 2008, in prep.
Caccianiga, A., Severgnini, P., DellaăCeca, R., et al. 2008, A&A, 477, 735
Cavaliere, A., & Vittorini, V. 2000, ApJ, 543, 599
Chapman, S. C., Barger, A. J., Cowie, L. L., et al. 2003, AJ, 585, 57
Chartas, G., Brandt, W. N., Gallagher, S. C., & Garmire, G. P. 2002, ApJ, 579, 169
Cirasuolo, M., Magliocchetti, M., & Celotti, A. 2005, MNRAS, 357, 1267
Cohen, J. G., Hogg, D. W., Blandford, R., et al. 2000, ApJ, 538, 29
Comastri, A. 2004, in Supermassive Black Holes in the Distant Universe, ed. A. J. Barger, Ap&SS Library, 308, 245 (Dordrecht Kluwer)
Comastri, A., Setti, G., Zamorani, G., & Hasinger, G. 1995, A&A, 296, 1
Cocchia, F., Fiore, F., Vignali, C., et al. 2007, A&A, 446, 31
Cowie, L. L., Songaila, A., Hu, E. M., & Cohen, J. G. 1996, AJ, 112, 839
Cowie, L. L., Barger, A. J., Bautz, M. W., Brandt, W. N., & Garmire, G. P. 2003, ApJ, 584, L57
Cowie, L. L., Barger, A. J., Hu, E. M., Capak, P., & Songaila, A. 2004, AJ, 127, 3137
Cristiani, S., Alexander, D. M., Bauer, F., et al. 2004, ApJ, 600, L119
Croton D. J., Springel, V., White, S. D., et. al. 2005, MNRAS, 365, 11
Daddi, E., Alexander, D. M., Dickinson, M., et al. 2007, ApJ, 670, 173
Della Ceca, R., Maccacaro, T., Caccianiga, A., et al. 2004, A&A, 428, 383
Della Ceca, R., Caccianiga, A., Severgnini, P., et al. 2008, A&A, 487, 119
Di Matteo, T., Croft, R. A. C., & Hernquist, L. 2003, ApJ, 593, 56
Di Matteo, T., Springel, V., & Hernquist, L. 2005, Nature, 433, 604
Eckart, M. E., Stern, D., Helfand, D., et al. 2006, ApJS, 165, 19
Faber, S. M., Willmer, C. N. A., Wolf, C., et al. 2007, ApJ, 665, 265
Fadda, D., Flores, H., Hasinger, G., et al. 2002, A&A, 383, 838
Fan, X., Strauss, M. A., Schneider, D. P., et al. 2001, AJ, 121, 54
Fan, X., Strauss, M. A., Schneider, D. P., et al. 2003, AJ, 125, 1649
Ferrarese, L., & Merrit, D. 2000, ApJ, 539, L9
Fiore, F., Brusa, M., Cocchia, F., et al. 2003, A&A, 409, 79
Fiore, F., Grazian, A., Santini, P., et al. 2008a, ApJ, 672, 94
Fiore F., Puccetti S., Brusa M., et al. 2008b, ApJ, submitted
Franceschini, A., Hasinger, G., Miyaji, T., & Malquori, D. 1999, MNRAS, 310, L5
Franceschini, A., Braito, V., & Fadda, D. 2002, MNRAS, 335, L51
Gebhardt, K., Bender, R., Bower, G., et al. 2000, ApJ, 539, L13
Gehrels, N. 1986, ApJ, 303, 336
Giacconi, R., Gursky, H., Paolini, F. R., & Rossi, B. B. 1962, Phys. Rev. Lett., 9, 439
Giacconi, R., Zirm, A., Wang, J. X., et al. 2002, ApJS, 139, 369
Giavalisco, M., Ferguson, H. C., Koekemoer, A. M., et al. 2004, ApJ, 600, L93
Gilli, R., Daddi, E., Zamorani, G., et al. 2005, A&A, 430, 811
Gilli, R., Comastri, A., & Hasinger, G. 2007, A&A, 463, 79 (GCH07)
Grazian, A., Fontana, A., de Santis, C. et al. 2006, A&A, 449, 951
Grossan, B. 1992, Ph.D. Thesis, MIT
Hammer, F., Flores, H., Elbaz, D., et al. 2005, A&A, 430, 115
Hasinger, G. 2004, Nucl. Phys. B, 132, 86
Hasinger, G., Altieri, B., Arnaud, M., et al. 2001, A&A, 365, L45
Hasinger, G., Schartel, N., & Komossa, S. 2002, ApJ, 573, L77
Hasinger, G., Miyaji, T. & Schmidt, M. 2005, A&A, 441, 417
Hasinger, G., Cappelluti, N., Brunner, H., et al. 2007, ApJS, 172, 29
Hopkins, P. F., Hernquist, L., Cox, T. J., et al. 2006, ApJ, 639, 700
Hopkins, P. F., Richards, G. T., & Hernquist, L. 2007, ApJ, 654, 731
Kauffmann, G., & Haehnelt, M. G. 2000, MNRAS, 311, 576
Kauffmann, G., Heckman, T. M., Budavári, T., et al. 2007, ApJS, 173, 357
Kormendy, J., & Richstone, D. 1995, ARA&A, 33, 581
La Franca, F., Fiore, F., Vignali, C., et al. 2002, ApJ, 570, 100
La Franca, F., Fiore, F., Comastri, A., et al. 2005, ApJ, 635, 864
Le Fevre, O., Vettolani, G., Paltani, S., et al. 2004, A&A, 428, 1043
Lehmann I., Hasinger G., Schmidt M., et al. 2000, A&A, 354, 35
Lehmer, B. D., Brandt, W. N., Alexander, D. M., et al. 2005, ApJS, 161, 21
Li, Y., Hernquist, L., Robertson, B. et al. 2007, ApJ, 665, 187
Lockman, F. J., Jahoda, K., & McCammon, D. 1986, ApJ, 302, 432
Madau, P., Ferguson, H. C., Dickinson, M. E., et al. 1996, MNRAS, 283, 1388
Magorrian, J., Tremaine, S., Richstone, D., et al. 1998, AJ, 115, 2285
Mainieri, V., Bergeron, J., Hasinger, G., et al. 2002, A&A, 393, 425
Mainieri, V., Rosati, P., Tozzi, P., et al. 2005, A&A, 437, 805
Mainieri, V., Kellermann, K. I., Fomalont, E. B., et al. 2008, ApJ, submitted
Maiolino, R., Mignoli, M., Pozzetti, L., et al. 2006, A&A, 445, 457
Maiolino, R., Shemmer, O., Imanishi, M., et al. 2007, A&A, 468, 979
Marconi, A., Risaliti, G., Gilli, R., et al. 2004, MNRAS, 351, 169
Martinez–Sansigre, A., Rawlings, S., Bonfield, D. G., et al. 2007, MNRAS, 379, L6
Menci, N., Fiore, F., Perola, G. C., & Cavaliere, A. 2004, ApJ, 606, 58
Menci, N., Fiore, F., Puccetti, S., & Cavaliere, A. 2008, in preparation
Merloni, A. 2004, MNRAS, 353, 1035
Merloni, A., & Heinz, S. 2008, MNRAS, in press, [arXiv:0805.2499]
Mignoli, M., Pozzetti, L., Comastri, A., et al. 2004, A&A, 418, 827
Mignoli, M., Cimatti, A., Zamorani, G., et al. 2005, A&A, 437, 833
Miyaji, T., Hasinger, G., & Schmidt, M. 2000, A&A, 353, 25
Mobasher, B., Idzi, R., Benitez, N., et al. 2004, ApJ, 600, L167
Moran, E. C., Filippenko, A. V., & Chornock, R. 2000, ApJ, 579, L71
Moretti, A., Campana, S., Lazzati, D., et al. 2003, ApJ, 588, 696
Müller, A., & Hasinger, G. 2007, in 2007 STScI spring symposium: Black Holes, M. Livio, & A. M. Koekemoer (Cambridge University Press), in press, [arXiv:0708.0942]
Nandra, K., Georgakakis, A., Willmer, C. N. A., et al. 2007, ApJ, 660, L11
Netzer, H., Mainieri, V., Rosati, P., Trakhtenbrot, B. 2006, A&A, 453, 525
Panessa, F., & Bassani, L. 2002, A&A, 394, 435
Perola, G. C., Puccetti, S., Fiore, F., et al. 2004, A&A, 421, 491
Piccinotti, G., Mushotzky, R. F., Boldt, E. A., et al. 1982, ApJ, 253, 485
Popesso, P., Dickinson, M., Nonino, M., et al. 2008, [arXiv:0802.2930]
Ranalli, P., Comastri, & A., Setti, G. 2003, A&A, 399, 39
Rhook, K. J., & Haehnelt, M. G. 2008, MNRAS, submitted [arXiv:0801.3482]
Richards, G., Strauss, M. A., Fan, X., et al. 2006, AJ, 131, 2766
Risaliti, G., Maiolino, R., & Salvati, M. 1999, ApJ, 522, 157
Rix, H.-W., Barden, M., Beckwith, S., et al. 2004, ApJS, 152, 163
Rosati P., Tozzi P., Giacconi R., et al. 2002, ApJ, 566, 667
Scannapieco, E., & Oh, S. P. 2004, ApJ, 608, 62
Schiminovich, D., Wyder, T. K., Martin, D. C., et al. 2007, ApJS, 173, 316
Schmidt, M., Hasinger, G., Gunn, J. E., et al. 1998, A&A, 329, 495
Shinozaki, K., Miyaji, T., Ishisaki, Y., Ueda, Y., & Ogasaka, Y. 2006, AJ, 131, 2843
Silk, J., & Rees, M. J. 1998, A&A, 331, L1
Silverman, J. D., Green, P. J., Barkhouse, W. A. et al. 2005, ApJ, 624, 630
Silverman, J. D., Mainieri, V., Lehmer, B. D., et al. 2008, ApJ, 675, 1025
Simpson, C. 2005, MNRAS, 360, 565
Smail, I., Chapman, S. C., Blain, A. W., & Ivison, R. J. 2004, ApJ, 616, 71

Sturm, E., Schweitzer, M., Lutz, D., et al. 2005, ApJ, 629, L21
Sturm, E., Hasinger, G., Lehmann, I., et al. 2006, ApJ, 642, 81
Swinbank, A. M., Smail, I., Chapman, S. C. et al. 2004, ApJ, 617, 64
Springel, V., Frenk, C. S., & White, S. D. M. 2006, Nature 440, 1137
Steffen, A. T., Barger, A. J., Cowie, L. L., Mushotzky, R. F., & Yang, Y. 2003, ApJ, 569, L23
Steffen, A. T., Barger, A. J., Capak, P., et al. 2004, AJ, 128, 1483
Szokoly, G. P., Bergeron, J., Hasinger, G., et al. 2004, ApJS, 155, 271
Szokoly, G. P. et al. 2008, in preparation
Tozzi, P., Gilli, R., Mainieri, V. et al. 2006, A&A, 451, 457
Treister, E., & Urry, C. M. 2005, ApJ, 630, 115
Treister, E., & Urry, C. M. 2006, ApJ, 652, L79
Treister, E., Urry, C. M., Chatzichristou, E., et al. 2004, ApJ, 616, 123
Treister, E., Krolik, J. H., & Dullemond, C. 2008, ApJ, 679, 140
Ueda, Y., Takahashi, T., Inoue, H., et al. 1999, ApJ, 518, 656
Ueda, Y., Ishisaki, Y., Takahashi, T., Makishima, K., & Ohashi, T. 2001, ApJS, 133, 1
Ueda, Y., Akiyama, M., Ohta, K., & Miyaji, T. 2003, ApJ, 598, 886
Ueda, Y., Ishisaki, Y., Takahashi, T., Makishima, K., & Ohashi, T. 2005, ApJS, 161, 185
Ueda, Y., Eguchi, S., Y., Terashima, Y., et al. 2007, ApJ, 664, L79
Vanzella, E., Cristiani, S., Dickinson, M., et al. 2008, A&A, 478, 83
Volonteri, M., Madau, P., Quataert, E., & Rees, M. J. 2005, ApJ, 620, 69
Wall, J. V., Jackson, C. A., Shaver, P. A., Hook, I. M., & Kellermann, K. I. 2005, A&A, 434, 133
Waddington, I., Windhorst, R. A., Cohen, S. H., et al. 1999, ApJ, 526, L77
Wang, J. X., Jiang, P., Zheng, Z. Y., et al. 2007, ApJ, 657, 95
Watson, M. G., Augueres, J.-L., Ballet, J., et al., A&A, 365, L51
Wirth, G. D., Willmer, C. N. A., Amico, P., et al. 2004, AJ, 127, 3121
Wolf, C., Meisenheimer, K., Kleinheinrich, M., et al. 2004, A&A, 421, 913
Worsley, M., Fabian, A. C., Mateos, S., et al. 2004, MNRAS, 352, L28
Wyithe J. S. B., & Loeb, A. 2003, ApJ, 595, 614
Yang, Y., Mushotzky, R. F., Steffen, A. T., Barger, A. J., & Cowie, L. L. 2004, AJ, 128, 1501
Zheng, W., Mikles, V. J., Mainieri, V., et al. 2004, ApJS, 155, 73